2.7 Ga plume associated VMS mineralisation in the Eastern Goldfields Superterrane: insights from the Ag-Zn-(Au) Nimbus deposit

Citation for published version:
Hollis, S, Mole, D, Gillespie, P, Caruso, S, Tessalina, S, Pumphrey, A, Barnes, S, Cas, R, Hildrew, C, Hancock, L, Yeats, C, Verbeeten, A & Wyche, S 2016, '2.7 Ga plume associated VMS mineralisation in the Eastern Goldfields Superterrane: insights from the Ag-Zn-(Au) Nimbus deposit', *Applied Earth Science*, vol. 125, no. 2, pp. 84-85. https://doi.org/10.1080/03717453.2016.1166634

Digital Object Identifier (DOI):
10.1080/03717453.2016.1166634

Link:
Link to publication record in Edinburgh Research Explorer

Document Version:
Peer reviewed version

Published In:
Applied Earth Science

2.7 Ga plume associated VHMS mineralization in the Eastern Goldfields Superterrane, Yilgarn Craton: insights from the low temperature and shallow water, Ag-Zn-(Au) Nimbus deposit

S.P. Hollis[1,2,3*], D. Mole[1], P. Gillespie[4], S.J. Barnes[1], S. Tessalina[5], R.A.F. Cas[7,8], C. Hildrew[8], A. Pumphrey[4], M.D. Goodz[9], S. Caruso[10], C.J. Yeats[11], A. Verbeeten[12], S.M. Belford[13], S. Wyche[2] & L.A.J. Martin[14]

[1]CSIRO Mineral Resources, 26 Dick Perry Avenue, Kensington, Western Australia, 6151, Australia

[2]Geological Survey Division, Department of Mines and Petroleum, East Perth, Western Australia, 6004, Australia

[3]iCRAG (Irish Centre for Research in Applied Geosciences), School of Earth Sciences, University College Dublin, Belfield, Dublin 4, Ireland. *E-mail: steve.hollis@icrag-centre.org

[4]MacPhersons Resources, Kalgoorlie, Western Australia, 6430, Australia

[5]John de Laeter Isotope Centre for Isotopic Research & The Institute for Geoscience Research (TIGeR), Curtin University, Kent St, Bentley, Western Australia, 6102, Australia

[7]School of Geosciences, Monash University, Victoria 3800, Australia

[8]ARC Centre of Excellence in Ore Deposits (CODES), University of Tasmania, Hobart, Tasmania, 7001, Australia

[9]Goodz & Associates GMC Pty Ltd, PO Box 10488, Kalgoorlie, Western Australia, 6430, Australia

[10]Centre for Exploration Targeting, The University of Western Australia, 35 Stirling Highway, Crawley, Western Australia, 6009, Australia

[11]Geological Survey of New South Wales, NSW Department of Industry, 516 High St, Maitland, New South Wales, 2320, Australia

[12]Minerex Petrographic Services, PO Box 548, Kalgoorlie, Western Australia, 6430, Australia

[13]Consulting Geologist, PO Box 1212, Fremantle, Western Australia, 6160, Australia

[14]ARC Centre of Excellence for Core to Crust Fluid Systems (CCFS) and Centre Microscopy Characterisation and Analysis, The University of Western Australia, Crawley, Western Australia, 6009, Australia

A manuscript for ***Precambrian Research***

Keywords: volcanic-hosted massive sulfide; Archaean; mantle plume; subduction; greenstone; oxygen isotope

Abstract

Economic volcanic-hosted massive sulfide (VHMS) deposits of the Archaean Yilgarn Craton of Western Australia are restricted to zones of juvenile crust as revealed through regional Nd, Pb and Hf isotopic variations and the geochemistry of felsic volcanic rocks. Interpreted as Archaean paleo-rift zones, one of these runs N-S through the Eastern Goldfields Superterrane (broadly coincident with the Kurnalpi Terrane) and is associated with the high grade ca. 2690 Ma Teutonic Bore, Jaguar and Bentley deposits, plus sub-economic VHMS mineralization further south. To date, only small historic Cu occurrences (e.g. Anaconda) and barren pyritic lenses have been recognised in the older >2.7 Ga plume-dominated lower stratigraphy of the Eastern Goldfields Superterrane.

The Nimbus Ag-Zn-(Au) deposit (12.1 Mt at 52 g/t Ag, 0.9% Zn and 0.2g/t Au) is located approximately 10 km east of Kalgoorlie, near the margin of the Kurnalpi Terrane. Its origin has been contentious for a number of years, with previous models favouring seafloor/sub-seafloor VHMS mineralization or a high sulfidation fault-hosted system. We present a detailed account of the deposit, its host stratigraphy and associated hydrothermal alteration, plus two new SHRIMP U-Pb zircon ages, Pb isotope (galena), and O isotope (zircon) constraints. Compared to other VHMS occurrences in the Yilgarn Craton, the Nimbus deposit is unusual in terms of its tectono-stratigraphic position, the geochemistry of its host sequence (i.e. FI-affinity felsic volcanic rocks, ocean-plateau-like low-Th basalts), mineralogy (e.g. abundance of Ag-Sb-Pb-As bearing sulfosalts, high Hg, low Cu) and quartz-carbonate-sericite dominated alteration assemblages. Classification of Nimbus as a shallow water and low temperature VHMS deposit with epithermal characteristics (i.e. a hybrid bimodal-felsic deposit) is consistent with its position near the margin of the Kurnalpi paleo-rift zone and radiogenic μ ($^{238}U/^{204}Pb$) values. The recognition that the Nimbus deposit is associated with c.

2705 Ma plume magmatism opens new areas for VHMS exploration in the Eastern Goldfields Superterrane over a strike length exceeding 500 km.

1. Introduction

Despite isolated successes in the 1970s, such as the discovery of significant orebodies at Golden Grove and Teutonic Bore, exploration for volcanic-hosted massive sulfide (VHMS) mineralization waned through most of the 1980s and 1990s in the Archaean Yilgarn Craton of Western Australia (Yeats, 2007). Although renewed exploration activity during the past decade has identified several new resources (e.g. Bentley, Just Desserts, Hollandaire), only a handful of deposits have been brought into production (Hollis et al., 2015; Fig. 1). Exploration challenges associated with regolith and deep cover exacerbate the already difficult task of exploring for small, deformed deposits in stratigraphically complex volcanic terranes. However, understanding the tectono-stratigraphic relationships of VHMS deposits in greenstone sequences greatly improves the effectiveness of mineral exploration (e.g. Belford et al., 2015; Hayman et al., 2015a; Duuring et al., 2016).

Significant VHMS resources of the Yilgarn Craton are largely restricted to two main zones of juvenile crust, as revealed through regional Nd, Pb and Hf isotopic variations (Ivanic et al., 2012; Huston et al., 2014; Mole et al., 2013, 2014; Fig. 2) and the geochemistry of felsic volcanic rocks (e.g. Brown et al., 2002; Barley et al., 2008; Hollis et al., 2015, in press). Interpreted as an Archaean paleo-rift zone that was reactivated several times, the Cue Zone of the northern Youanmi Terrane (Huston et al., 2014; Fig. 2a) is associated with at least three episodes of VHMS mineralization (reviewed in Hollis et al., 2015):

(i) an initial stage, dated from ca. 2980 Ma to ca. 2930 Ma, in bimodal to dominantly felsic greenstone belts (e.g. Mt. Gibson, Golden Grove, Weld Range: Yeats & Groves, 1998; Sharpe & Gemmell, 2002; Guilliamse, 2014);

(ii) at ca. 2815 Ma, during the eruption of the plume-related Norie Group and coeval with the emplacement of at least five large igneous complexes at shallow levels in the crust (e.g. Austin-Quinns, Just Desserts: Ivanic et al., 2010; Hassan, 2014; Duuring et al., 2016);

(iii) from ca. 2760 to ca. 2745 Ma during the deposition of the Greensleeves Formation (e.g. Hollandaire, Dalgaranga, Mt. Mulcahy: Hayman et al., 2015a).

An additional VHMS event in the northeast Youanmi Terrane at ca. 2725 Ma appears to be restricted to the Gum Creek greenstone belt (Hollis et al., 2015, in press). This age is coincident with Yalgowra Suite mafic magmatic event (Ivanic et al., 2010), rift development further west in the Glen Group (Van Kranendonk et al., 2013) and Marda Complex, and the onset of plume magmatism in the Eastern Goldfields Superterrane (Hayman et al., 2015b).

A second Archaean paleo-rift zone in the Yilgarn Craton runs N-S through the Kurnalpi Terrane in the Eastern Goldfields Superterrane (Huston et al., 2014), which is the focus of this paper. The relationship between this area of juvenile crust and Cu-Zn mineralization is evident in Figure 2, with significant resources mined around Teutonic Bore (Hallberg & Thompson, 1981; Huston et al., 2014; Belford et al., 2015) and smaller base metal occurrences further south (e.g. Jungle Pool, King/Erayinia) (Hollis et al., 2015). The ca. 2692 Ma Teutonic Bore Volcanic Complex hosts the high-grade Teutonic Bore, Jaguar and Bentley deposits. Mineral occurrences at Tuff Hill, Mason Hill and Fisher Well to the northeast (Fig. 2) occur in the Burtville Terrane (Ferguson, 1999) which has a similar age and stratigraphy to the Youanmi Terrane (Pawley et al., 2012).

The Nimbus Ag-Zn-(Au) deposit (12.1 Mt at 52 g/t Ag, 0.9% Zn and 0.2g/t Au) is located approximately 265 km south of Teutonic Bore and 10 km east of Kalgoorlie, near the mapped boundary between the Kalgoorlie and Kurnalpi terranes (Fig. 1). Its origin has been debated for a number of years, with previous workers favouring either seafloor/sub-seafloor VHMS mineralization (e.g. Mulholland et al., 1998; Doyle, 1998; Belford, 2011), or a fault-hosted high-sulfidation system (Henderson et al., 2012). Its Ag-rich nature is unique in the

Yilgarn Craton. We present a detailed account of the deposit, including new constraints on its age, mineralogy, geochemistry, host stratigraphy, tectonic setting, and the style of hydrothermal alteration. Implications for VHMS exploration in the Eastern Goldfields are discussed.

2. Regional geology

The geology of the Yilgarn Craton with respect to VHMS mineralization has recently been reviewed by Hollis et al. (2015). Here we focus on the stratigraphy of the western half of the Eastern Goldfields Superterrane - the Kalgoorlie and Kurnalpi terranes (Fig. 1).

The geology of the Kalgoorlie Terrane is broadly divisible into the lower 2720-2690 Ma mafic-ultramafic Kambalda Sequence (Beresford et al., 2005) and the overlying 2690-2660 Ma Kalgoorlie Sequence (Krapež & Hand, 2008) (Fig. 3a). At least two cycles of plume related magmatism have recently been recognized in the lower mafic-ultramafic sequence (Hayman et al., 2015b; Fig. 3b). Cycle 1 lasted from ca. 2720 to 2705 Ma and was restricted to the western half of the Kalgoorlie Terrane (i.e. Agnew, Ora Banda and Coolgardie: Hayman et al., 2015b; Fig. 3b). This event was contemporaneous with komatiitic magmatism in the Wattagee Formation of the Youanmi Terrane (Fig. 1; Van Kranendonk et al., 2013) and the emplacement of the mafic Yalgowra Suite throughout the Cue Zone (Fig. 2; Ivanic et al., 2010). Cycle 2 magmatism was a regional event across the Kalgoorlie Terrane and lasted from ca. 2705 to 2690 Ma (Hayman et al., 2015b; Fig. 3b). Plume-related komatiitic cumulate bodies host world-class Ni resources such as Mt. Keith and the Kambalda camp, and are interpreted to be the products of high-flux komatiite volcanism focused along the eastern margin of the Youanmi Terrane (Barnes, 2006; Barnes & Fiorentini, 2012; Mole et al., 2014). Overlying mafic rocks of each cycle were derived from the extensive crystal fractionation and crustal contamination of plume derived magmas in mid-crustal magma chambers (Barnes et al., 2012; Hayman et al., 2015b). The 2690-2660 Ma Kalgoorlie Sequence comprises a >3 km thick package of volcaniclastic rocks, felsic to intermediate volcanic rocks, and mafic intrusive complexes with minor mafic volcanic rocks (Squire et al., 2010; Fig. 3a). Most volcaniclastic rocks of the Kalgoorlie Sequence formed by deposition from turbidity currents (Krapež & Hand, 2008). Late doming and extension associated with the emplacement of a widespread high-Ca tonalite-trondjhemite-granodiorite (TTG) suite produced the late quartz-dominated clastic basins (Wyche et al., 2013; Fig. 3a).

Broadly coeval with the Kambalda Sequence of the Kalgoorlie Terrane, the Kurnalpi and Minerie sequences of the Kurnalpi Terrane are represented by a more intermediate package of rocks (Fig. 3a). Although some workers have attributed the Kurnalpi andesites to an Archaean arc (e.g. Barley et al., 2008; Czarnota et al., 2010), they are also geochemically consistent with the fractionation of plume-related tholeiitic basalts, coupled with their contamination by contemporaneous partial melts of preexisting continental crust (Barnes & Van Kranendonk, 2014; see Discussion). Compared to modern island arc andesites these rocks contain unusually high concentrations of MgO, Ni and Cr (Barnes & Van Kranendonk, 2014). Between 2692 and 2680 Ma, volcanic centres in the Kurnalpi Terrane (Gindalbie Domain and further south; Fig. 1) are associated with largely bimodal (basalt-rhyolite) volcanic and associated sedimentary rocks, although some contain significant volumes of andesites (Fig. 3a). The felsic rocks are significantly enriched in the high field strength elements (HFSE) and heavy rare earth elements (HREE) (Brown et al., 2002; Barley et al., 2008; Hollis et al., 2015), diagnostic of shallow crustal melting (Lesher et al., 1986; Piercey et al., 2001; Hart et al., 2004). Significant VHMS resources occur around Teutonic Bore, with geochemically similar felsic volcanic rocks identified throughout the Kurnalpi Terrane (e.g. Bore Well, Melita: Hollis et al., in press).

The Ag-Zn-(Au) Nimbus deposit lies in the Boorara Domain of the Kalgoorlie Terrane (Cassidy et al., 2006), in a package of rocks bound to the west and east by the Boorara and Kanowna shear zones (Fig. 4). The regional geology of the Boorara Domain is similar to that elsewhere in eastern half of the Kalgoorlie Terrane (Swager, 1997; Trofimovs et al., 2004, 2006; Fiorentini et al., 2010). Regional correlations for the stratigraphy around Black Swan (in the southern part of the domain) and Mount Keith (to the north) are presented in Figure 3b. In both areas komatiites were erupted contemporaneously with dacite, with clear evidence for magma mingling (Rosengren et al., 2008; Cas et al., 2013; Barnes & Van Kranendonk, 2014). No stratigraphy has been published for the Nimbus area and it was previously (incorrectly) believed that the local stratigraphy formed part of the Black Flag Group due to similarities in lithology (Fig. 3a).

3. Stratigraphy

Although hydrothermal alteration, tectonic deformation and deep weathering obscure much of the primary mineralogy at Nimbus, relict volcanic textures are well preserved in diamond drillcore, and in saprolite of the Discovery and East pit walls. Mineralization occurs in a NW (to NNW) trending and steeply-dipping, bimodal-felsic package of volcanic rocks (quartz-feldspar-phyric dacite and lesser basalt, plus their autoclastic equivalents) with subordinate black carbonaceous mudstone, tuffaceous volcaniclastic sandstone, polymict conglomerates and volcanic breccias. The local stratigraphy is dominated by rocks of dacitic composition (Fig. 5a). Spinifex textured komatiite flows, volcanic sandstones/siltstones, polymict volcanic breccias, carbonaceous mudstone, dolerite and basalt were intersected in distal drillhole BODH015 (Fig. 4). All rocks described here have been subjected to lower greenschist facies metamorphism. A more detailed account of the Nimbus stratigraphy to that detailed below (including comprehensive facies logging) will be presented elsewhere by Hildrew et al. (in prep; based on Hildrew, 2015).

Facing: Debate continues on whether the Nimbus stratigraphy youngs to the NE or SW, due to a lack of diagnostic way-up indicators. Only in drillholes NBDH010 (Fig. 5a) and BODH015 have unequivocal younging directions been observed by the authors (Fig. 6a-c). In drillhole BODH015, ~1 km SW of the deposit, a fold axis is clear in the core, with several >2 m thick graded beds in the top half younging up hole (Fig. 6b). In the lower half of the core, flame structures, cross-bedding (Fig. 6c), erosional bases and grading indicate this part of the sequence is overturned.

Evidence for a SW younging direction is restricted to drillhole NBDH010 (Fig. 5a), where a thin (5 cm) of grading in a turbidite interbedded with black mudstone (Fig. 6a) forms one of several narrow bands of sediment in a 275 m thick sequence of mafic rocks (the Northeast basalt: Fig. 4). Mafic rocks either side of the graded bedding display distinct immobile element ratios (e.g. Zr/Cr, Cr/Al at ~204m; see Fig. 7) suggesting that they represent separate units and not a folded sequence. By contrast, evidence for a NE younging direction was presented by Doyle (1998) from hole SHD002. Normal grading with mudstone, intraclasts of mudstone, and crystal-rich bases were taken as evidence that the sequence faces NE (Doyle, 1998). Other less robust evidence favouring a model whereby the stratigraphy youngs to the NE, includes: (i) an increased concentration of Cu-Au to the SW in the deposit (as Cu is more common in the feeder zones of VHMS systems; Franklin et al., 2005), and (ii) that the polymict conglomerates to the NE contain clasts of variably hydrothermally-altered dacite and are only themselves weakly mineralized. Due to the unclear facing, we refer to the current geographic position of the units, rather than their stratigraphic position.

Local stratigraphy: Immediately NE of the Nimbus deposit, a thick sequence of dacitic volcaniclastic sandstones, volcanic breccias and polymict conglomerates have been recognised. These units are best observed in the top of drillhole NBDH010 (Fig. 4) where the former two lithologies are preserved as saprolite and saprock. The polymict conglomerates (>125m thick in hole NBDH010) are composed of rounded to sub-angular dacite clasts and angular fragments of carbonaceous mudstone in a poorly sorted matrix of varying dacitic to graphitic composition (Figs. 6d-e). Dacite clasts are dense, non-vesicular and show various degrees of crystallinity and hydrothermal alteration. At least five broad pulses of sedimentation have been identified, through systematic variations in the composition of the dominant clast type, matrix, and maximum clast size with depth. These pulses coincide with shifts in immobile element profiles (e.g. Sc/V, V/Al, Zr/Y; see Fig. 7). The polymict conglomerates are interpreted to represent pulsing debris flow units from a subaerial shoreline into a deeper anoxic basin (as described by Hildrew, 2015). The overall massive and poorly sorted character indicates deposition from mass flow processes. The rounded character of clasts requires a sub-aerial environment (beach or fluvial setting), such as for an emergent dome/stratovolcano.

Large thicknesses of intensely hydrothermally-altered quartz-feldspar porphyritic dacite dominate the Nimbus stratigraphy. Due to the intense hydrothermal alteration throughout the coherent dacite facies (Fig. 6f) it is unclear if the thick drill intercepts are composed of one or more flows/domes/intrusions. Individual units cannot be distinguished geochemically using immobile element ratios (see Geochemistry). Along the margin of dacite units, monomict, dominantly clast-supported blocky breccias, interpreted to be hyaloclastite (Fig. 6g), often grade into jigsaw-fit breccias. Sharp edges and blocky to curviplanar fragments (e.g. NBDH035; Fig. 6h) are indicative of quench fragmentation (described in Hildrew et al., in prep). In addition, the dacite units may be pervasively hydraulically fractured. Both of these lithologies (quench fragmented and hydraulically fractured dacite breccias) are often intensely mineralized and altered, with fractures providing suitable pathways for hydrothermal fluids (e.g. Cas et al., 2011; see Discussion). In some drillholes carbonaceous mudstone has infiltrated the matrix to these breccias, indicating peperite origins (Doyle, 1998; Belford, 2011).

Mafic rocks are largely absent under the Discovery Pit, but occur in and under the East Pit with several units observed to date (referred to as the Northeast, East Pit, Au150, Western and Office basalts; Fig. 4). These rocks represent the ‘andesites’ of earlier workers that were suggested to be intrusive (Doyle, 1998; Belford, 2011). Conventional whole rock geochemistry of drillcore presented here demonstrate these rocks are mafic in composition (e.g. Pearce, 1996; Hastie et al., 2007). These rocks are fine-grained, variably plagioclase-phyric and have been subjected to variably intense quartz-albite-carbonate-chlorite alteration, accompanied by networks of hydraulic fractures. Peperitic upper and lower contacts for mafic rocks with carbonaceous mudstone were observed in several drillholes (e.g. NBDH010; Fig. 6i), suggest they represent very shallow, syn-depositional invasive flows or perhaps more likely, sills. Abundant hyaloclastite (Fig. 6j) and varioles (Fig. 6k) are indicative of magma-water interaction and an originally glass groundmass respectively. No definitive examples of pillow lavas were observed, except possibly at the top of hole BOD202 (Western basalt) which is also associated with a polymict mafic breccia (Fig. 6l).

Thin (~1 m thick) beds of black carbonaceous mudstone (variably pyritic and often intensely silicified; Fig. 6m) occur throughout the Nimbus stratigraphy - most often in the uppermost levels. This rock type represents ambient background sedimentation, indicative of an anoxic environment below storm wave base. Intercalated sandstone units were suggested by Doyle (1998) to form via low-density turbidity currents.

Distal stratigraphy: In regional exploration drillhole BODH015, approximately 1km SW from Nimbus, a folded sequence of basalt, Au-bearing dolerite, polymict volcanic breccias

(Fig. 6n), spinifex-textured komatiite flows (Fig. 6o-p), carbonaceous mudstone, and a mixed sequence of volcanic siltstones and sandstones was intersected. Further detail and their genetic implications for depositional environment is provided by Hildrew et al. (in prep).

4. Mineralization

The Ag-Zn-(Au) Nimbus deposit includes multiple lenses of primary sulfide mineralization, and overlying zones of oxide and supergene mineralization. Between 2003 and 2006, deeply weathered oxide and supergene ('transition') material was mined by Polymetals WA from two small open pits (Discovery and East) for a total production of 0.32 Mt at 352 g/t Ag (including 6.5t Hg; described in Mulholland et al., 1998). The Nimbus resource of primary sulfide mineralization (Fig. 5a) currently stands at 12.1 Mt at 52 g/t Ag, 0.9 % Zn and 0.2 g/t Au (including measured, indicated and inferred resources; April, 2015). Several lodes of high grade silver-zinc (1.22 Mt at 175g/t Ag and 3.5% Zn) and anomalous gold (2.45 Mt at 0.8 g/t Au) mineralization have been identified. The mineralogy of the deposit has been partially described in a number of unpublished company/consultancy reports (Townend, 1996; Mulholland et al., 1998; Doyle 1998; Powell, 1999; McArthur, 2006; Marjoribanks, 2012; Crawford, 2012, McArthur, 2012). This information is compiled and expanded upon here. A short summary is provided below, with additional detail in Supplementary Information.

Primary Ag-Zn sulfide mineralization at Nimbus occurs as a series of stacked, steeply plunging and subparallel lenses (Fig. 5). Several units of early well-developed massive pyrite (Fig. 8a), typically 2 to 7m thick, have clearly replaced glassy quartz-plagioclase phyric dacite, as recognized by a number of earlier workers (Doyle, 1999; Belford, 2011; Crawford 2012). In some drillholes multiple horizons of massive pyrite are present with discordant zones of stringer pyrite and sphalerite occurring between these in a coherent dacite facies. Although a number of earlier workers described the pyrite as colloform in nature this term is not strictly correct, as the Nimbus massive pyrite occurs through replacement and not through precipitation in open space. Underlying these lenses of barren massive pyrite, polymetallic sulfide mineralization typically occurs as: 1) semi-massive (Fig. 8e), stringer and breccia-type Ag-Zn±Pb-(Cu-Au) sulfides (Figs. 8f-g) associated with monomict dacite breccia (which may have focussed hydrothermal fluids – see Discussion); and 2) as discordant stringer and disseminated sphalerite-pyrite in coherent dacite (Figs. 8h-l).

Where well preserved, the early 'colloform' pyrite occurs with radial fibrous and concentrically banded textures with interstitial quartz and/or carbon (Doyle, 1998). The latter was subsequently fragmented at all scales by quartz-pyrite due to hydraulic brecciation, with repeated crack-seal events recognized by Crawford (2012). Following this, all phases were brecciated and replaced by straw-yellow Fe-poor sphalerite. This early sphalerite can contain rare flecks of chalcopyrite, galena and/or rare arsenopyrite (in order of decreasing abundance). Although, galena is typically younger than low-Fe sphalerite (brecciating and replacing both low-Fe sphalerite and all early pyrite phases), both are also frequently intergrown. When present in significant quantities galena is also intergrown with a diverse suite of Ag-Sb-Pb-As-(Cu) sulfosalts (the main ore phase), such as (in order of decreasing abundance): boulangerite [$Pb_5Sb_4S_{11}$], pyrargyrite [Ag_3SbS_3], Ag-bearing tetrahedrite [$(Cu,Fe,Zn,Ag)_{12}Sb_4S_{13}$], marrite [$AgPbAsS_3$], bournonite [$PbCuSbS_3$], and rare owyheeite [$Pb_7Ag_2(Sb,Bi)_8S_{20}$] (e.g. Townend, 1996; Crossley, 2011; Crawford, 2012). McArthur (2006, 2012) identified covellite [CuS], and sulfosalts enargite [Cu_3AsS_4] (associated with chalcopyrite) and freibergite [$(Ag,Cu,Fe)_{12}(As,Sb)_4S_{13}$] from rock chips in holes NBRC202 and NBRC203 (samples represented by blue bars in Fig. 5a). Coarser patches of a younger generation of chalcopyrite are also associated with the high-grade Ag-Pb-Zn main ore phase. Fe-rich sphalerite always appears to be younger than the low-Fe phase, and appears to have precipitated with galena and the various sulfosalt minerals during the main ore phase - though in some instances post-dates it.

Mafic rocks at Nimbus are typically weakly mineralized, containing only minor amounts of disseminated pyrite and low-Fe sphalerite, and very rarely trace chalcopyrite. Recent RAB drilling intercepted Au-rich mineralization in the Au150 basalt (NBRC167: e.g. 10 m at 4.1 g/t Au) with rock chips containing abundant pyrite, sphalerite and galena.

5. Hydrothermal alteration

Hydrothermal alteration at Nimbus is dominated by the extensive quartz-sericite±carbonate alteration of dacite and quartz-carbonate-chlorite alteration of mafic rocks. Representative photographs from drillcore are shown in Figure 9, with thin section photomicrographs presented in Supplementary Figure 1.

Coherent dacitic rocks at Nimbus comprise a broadly even distribution of quartz and plagioclase phenocrysts in a finely crystalline matrix. Phenocrysts may be fractured and broken (particularly quartz) and variably replaced by a combination of quartz, sericite, carbonate and minor chlorite. The groundmass is typically foliated and altered by a combination of quartz, sericite/muscovite, carbonate, chlorite and albite, with minor fuchsite, epidote, and carbon (discounting the regolith zone). Trace amounts of rutile, zircon and tourmaline also occur. Hydrothermal alteration is most intense surrounding sulfide mineralization. Well preserved volcanic textures occur distal to mineralization, where albite is increasingly common (Doyle, 1998). Rare arcuate and concentric shapes described by Doyle (1998) are consistent with perlite (i.e. a formerly glassy matrix). Albite is present in minor amounts throughout the host dacite, but is most abundant outside the main zone of quartz-sericite alteration (Doyle, 1998).

Where observed in drillcore, contacts between intensely silicified, sericitized and carbonate-altered dacitic rocks are often sharp, confirmed by sudden shifts in pXRF and whole rock geochemical K_2O and CaO contents (see Fig. 7). According to Doyle (1998) the sericite-carbonate altered zones enclose sericite-quartz alteration, with both alteration assemblages forming prior to the later sericite-carbonate-chlorite-fuchsite phase. Intense chloritization of dacite is predominantly restricted to narrow zones (Fig. 9e) and contacts with mafic rocks (Fig. 9g). In the pervasive chlorite zones, phenocrysts are barely visible. Near contacts with mafic rocks, anatomising networks of fuchsite-sericite-carbonate veinlets together with silicification produce pseudobreccia textures over tens of metres. In zones of high strain, augen of quartz-sericite-carbonate altered dacite are often enclosed in intensely foliated sericite-carbonate-fuchsite-chlorite altered dacite (Fig. 9g-h). Late anastomosing veinlets of yellow-green sericite (Fig. 9j) cut all earlier phases, and are in turn cut by quartz-carbonate±chlorite veins that host minor amounts of base metal sulfides (pyrite>galena-sphalerite>>chalcopyrite).

In the monomict dacite breccia facies, clasts are porphyritic and display evidence for quench fragmentation (including various stages of disintegration – described in Hildrew et al. in prep). The matrix is often intensely altered by quartz-sericite-chlorite-carbonate, more so than the clasts. When present, sulfide mineralization occurs first as disseminations in the matrix, then as a network of fine stringers, before finally replacing the clasts (Fig. 8d-e).

Mafic rocks at Nimbus comprise relic sericite-altered plagioclase laths and minor leucoxene, Fe-oxides and pyrite, with interstitial albite, sericite, quartz, carbonate, chlorite and fuchsite. In hyaloclastite, the matrix is often intensely altered leaving well-preserved igneous textures in the clasts (Supplementary Fig. 1f). By contrast, in coherent mafic rocks, nearly all primary textures have been destroyed by hydrothermal alteration (Supplementary Fig. 1g-h).

Thin zones of sedimentary chert have also been described from Nimbus by several workers (e.g. Marjoribanks, 2012), with an apparent banding of quartz-carbon (Fig. 9k). Thin sections examined containing 'chert' are related to the intense silicification of dacite and black shale, as described by Doyle (1998) and Belford (2011). Other sections of core contain irregular patches of dark cryptocrystalline silica with textures indicative of precipitation in open space (Fig. 9i).

6. Whole rock geochemistry

6.1. Methods

A total of forty-seven samples were analysed from diamond drillcore across the Nimbus stratigraphy (holes BOD0202, NBDH010, NBDH013, NBDH024 and NBDH035; see Fig. 5 for locations) and distal drillhole BODH015. Samples were submitted to two laboratories for analysis. Thirty-two (IG-prefixed) samples were powdered using a tungsten carbide mill and submitted to Intertek Genalysis, Perth, Western Australia. A further fifteen (ALS-prefixed) samples were submitted to ALS Laboratories, Perth. Further detail on digestion techniques, analytical methods, accuracy and precision are presented as Supplementary Information. Data is presented in Supplementary Table 1. A detailed discussion of the mobile element geochemistry in relation to hydrothermal alteration and mineralization is beyond the scope of this work and will be presented elsewhere (Hollis et al. in prep). A brief summary is presented in the Supplementary Information.

6.2. Immobile element geochemistry

All mafic volcanic rocks from Nimbus (including those intercepted in distal drillhole BODH015) are geochemically similar, characterised by low Zr/Y and Nb/Y ratios (i.e. subalkaline and tholeiitic compositions; Fig. 10a), flat REE profiles (La/Yb 0.9-2.4; Fig. 10g), and an absence of pronounced negative Nb anomalies on multi-element variation diagrams. Samples display either weakly developed negative or positive Eu anomalies (Fig. 10g), reflecting the mobility of this element in high temperature and/or reducing hydrothermal fluids (Sverjensky, 1984). Comparison of the Nimbus mafic rocks to the dataset of Barnes et al. (2012), who compiled whole-rock geochemical data from across the Eastern Goldfields, highlights their similarity to the low-Th tholeiite suite (Fig. 11b-d) – which includes the 2.7 Ga plume head Lunnon basalt and Golden Mile Dolerite (~20 Myr younger). Mafic rocks from Nimbus are plotted on various tectonic discrimination diagrams in Figure 11. Although samples straddle the MORB and BABB (backarc basin basalt) fields (Fig. 11a-b), their geochemical characteristics are also consistent with plume-head lavas (see Discussion). On the Th/Yb vs. Nb/Yb diagram of Pearce (1983), Nimbus mafic rocks plot between nMORB and eMORB just above the mantle array, due to elevated Th/Yb values - either a consequence of subduction zone processes or crustal contamination (Fig. 11c; see Discussion).

Felsic volcanic and volcaniclastic rocks analysed from Nimbus are of FI affinity according to the VHMS fertility classification diagrams of both Lesher et al. (1986; Fig. 10e) and Hart et al. (2004; Fig. 10f). These rocks display steep TTG-like REE profiles (La/Yb 21.7-107.0; Fig. 10h), pronounced negative Nb anomalies, high Th/Yb and Zr/Y, and very low HFSE concentrations (e.g. ~3ppm Y, <0.5ppm Yb). Felsic geochemical data from the Teutonic Bore and Jaguar VHMS deposits are plotted for comparison to the Nimbus dacite in Figure 10i. Two samples of brecciated dacite from Nimbus have low La/Yb ratios (5.8-6.3; Fig. 10h) – possibly a consequence of LREE mobility during hydrothermal alteration or the accidental incorporation of minor sedimentary material (i.e. peperite).

Samples of dacite clasts from the polymict conglomerates intersected in drillhole NBDH010 and volcanic sandstones from distal diamond drillhole BODH015 are geochemically indistinguishable to samples of dacite which host the Nimbus deposit. Slightly higher trace element concentrations on multi-element variation diagrams (Fig. 10h) are due to weaker mass gains of the major elements, and consequently a reduced dilution of the immobile trace elements. Bulk geochemical shifts in immobile ratios of the polymict conglomerates show variations in Sc/V, Zr/Y, V/Al and Cr/Al ratios (see Fig. 7) which reflects the pulsing of the debris flows with varying amounts of incorporated dacitic and sedimentary material (Fig. 6d-e).

Komatiites intersected in drillhole BODH015 are depleted in the LREE respective to the HREE, with flat HREE profiles (Fig. 10g). Discrimination between Barberton- and Munro-type komatiites can be achieved using Al_2O_3/TiO_2 and $(Gd/Yb)_N$ ratios (e.g. Arndt and Lesher, 2004). Al_2O_3/TiO_2 (21.0 to 22.2) and Gd/Yb_N ratios (1.03-1.33) for samples from hole BODH015 are similar to those of Al-undepleted Munro-type komatiites (Al_2O_3/TiO_2 ~20; Gd/Yb_{CN} ~1.0), common in the Eastern Goldfields Superterrane.

7. SHRIMP U-Pb zircon geochronology

7.1 Methods

Several large ~10 kg samples were collected from diamond drillcore for U-Pb zircon SHRIMP geochronology to determine if the host stratigraphy formed part of the 2670-2690 Ma Black Flag Group (which has similar lithologies and mafic units of low-Th tholeiitic composition; Hayman et al. 2015b) as previously believed by mine geologists. Approximately 2–3 kg of least-altered sample was processed for mineral separation at Geotrack Pty Ltd in Melbourne, Victoria. Zircons were separated using standard techniques and mounted on 25 mm diameter epoxy-resin mounts with chips of M257 zircon (main U/Pb calibration standard, 561.3 Ma, 840 ppm ^{238}U; Nasdala et al., 2008), NBS610 glass, OGC-1 (Pilbara granite zircons, $^{207}Pb/^{206}Pb$

age 3465 Ma, equivalent to OG1 of Stern et al., 2009; Supplementary Figure 2) and TEMORA (417 Ma; Black et al., 2003). Only samples of dacite yielded sufficient zircon for analysis. Two samples were dated: dacite from drillhole NBDH010 under the East Pit (sample NIM011, 491-494m) and dacite from drillhole NBDH035 under the Discovery Pit (SPHGEO1, 285.4-288.5m). Isotopic analyses were performed on the SHRIMP II instrument at the John de Laeter Centre of Mass Spectrometry at Curtin University. Further detail is provided as Supplementary Information.

7.2 Results

Zircons from samples NIM011 and SPHGEO1 display euhedral to subhedral igneous habit, with some angular anhedral grains likely representing fragments of larger, more euhedral grains. All zircons are similar in size at around 100-200 μm long and 100 μm wide, brown-clear in transmitted light, and display igneous textures (e.g. oscillatory zoning). Most grains appear pristine and evidence of metamictisation, such as darkening of grains or zones in BSE images, is rare, although cracks of varying size occur in many zircons.

Nimbus East Pit dacite. Twenty-six analyses on 22 grains were performed on zircons from sample NIM011. Eight analyses were removed. Four due to poor spot placement (i.e. the spot was placed on cracks resulting in analyses demonstrating Pb-loss) and four due to relatively low UO/U ratios suggesting U fractionation on analysis. The remaining 18 analyses yield a single concordant group (all analyses are ≤6% discordant). Due to the high concordance, a weighted mean age was used, yielding an age of 2702 ± 4 Ma (MSWD 0.91; Fig. 12a). The age is interpreted as the crystallisation age of the dacite.

Nimbus Discovery Pit dacite. Twenty-six analyses on 25 grains were performed on zircons from SPHGEO1. Four analyses were removed. Two due to poor spot placement and two due to high common Pb (>1%) (Table 1). The remaining 22 analyses yield a single concordant group (all analyses are ≤5% discordant). Due to the high concordance, a weighted mean age was used, yielding an age of 2703 ± 5 Ma (MSWD 2.2; Fig. 12b). It should be noted that analysis 15-1 (core), dated at 2804 ± 28 Ma, was removed due to f206 (percentage of common ^{206}Pb) of 1.4 and may represent an inherited zircon (Fig. 12b). Although an f206 value of 1.4 warrants removal, it is unlikely to significantly alter the age of the grain, suggesting this may be accurate. The data for the rim of this grain (15-2) yielded an age of 2687 ± 32 Ma (2σ) and is part of the crystallization event. Although the MSWD for sample SPHGEO1 is higher than preferred, no further analyses could be removed as no problems were identified with the data or grains. The slight spread in ages is interpreted as a small amount of U-Pb mobility due to the Archean age of the sample and its proximity to a hydrothermal system. The probability density plot demonstrates that this sample is essentially unimodal. An alternative explanation is that analysis 21-1, which yields a slightly anomalous age at 2727 ± 16 Ma, may be a xenocryst. Removal of this analysis produces an age of 2701 ± 5 Ma (MSWD 1.8). As there is no direct physical evidence to support this, the first age is interpreted as the crystallisation age of the dacite.

8. O isotopes

8.1. Methods

Oxygen isotope analysis of dated zircons was completed to help characterize the formation of the Nimbus dacite. Oxygen isotope ratios ($^{18}O/^{16}O$) in zircon were determined in samples NIM011 and SPHGEO1 via secondary ion mass spectrometry (SIMS) using a Cameca IMS 1280 multi-collector ion microprobe at the Centre for Microscopy, Characterisation and

Analysis (CMCA), University of Western Australia (UWA). The sample mount was re-polished to remove SHRIMP analytical pits before cleaning with detergent, distilled water and ethanol in an ultrasonic bath. Samples were coated with gold (30 nm in thickness) prior to SIMS analyses. Instrument setup, conditions for analysis, accuracy and precision are described fully in the Supplementary Information. Raw $^{18}O/^{16}O$ ratios and corrected $\delta^{18}O$ (quoted with respect to Vienna standard mean ocean water or V_{SMOW}) are presented in the Supplementary Table 2 and Figure 13.

8.2. Results

Nineteen $^{18}O/^{16}O$ SIMS analyses were performed on 17 zircons from NIM011 (Nimbus East Pit dacite; Figure 13). Two analyses were removed due to U-Pb discordance >5% (23-2, 10-1) and one as a significant outlier (34-1) related to high DTFA value (>40) at this analytical locality (on the limit of acceptable field centering parameters). All grains had been previously dated by SHRIMP, apart from grain 20. Data from this grain was within error of all other analyses and hence was not discarded. The results of $\delta^{18}O$ analyses of these grains range from 5.85±0.34‰ to 6.13±0.35‰ and indicate a homogenous single, uniform population in terms of $\delta^{18}O$, with a weighted mean value of 5.99±0.09‰ (2σ; MSWD 0.29). This error is unlikely to be representative based on individual spot errors, but the MSWD does demonstrate the excellent grouping between the data. A more realistic group $\delta^{18}O$ value for the zircons of NIM011 can be acquired by using the median value that accounts for any possible non-normal behaviour in the data. This yields a $\delta^{18}O$ value of 5.98±0.19‰ (2σ) (Fig. 13c). The error on this value is simply the standard deviation of the $\delta^{18}O$ analytical data, and is more realistic given the individual spot errors. The data range from the 'normal' mantle zircon range into slightly enriched $\delta^{18}O$ compositions. The median value is slightly enriched relative to, but within error of, typical mantle $\delta^{18}O$ values. Despite these slightly enriched values, the median, weighted mean, and all 16 analyses are within error of the mantle value and also <6.5‰; considered the maximum accepted value for mantle-derived components (Cavosie et al., 2005; Kemp et al., 2006).

Nineteen analyses were performed on 18 zircons from SPHGEO1 (Nimbus Discovery Pit dacite; Fig. 13). Three analyses were removed due to correlations between slightly lower $\delta^{18}O$ values (5.69‰ and 5.58‰; compared to main group), common-Pb >1% (15-1), and low Th/U (0.025, 15-2). These data suggest grain 15 has slight crystal lattice damage. Analysis 17-1 was removed due to cracking in and around the analysis site. The remaining 16 analyses were all performed on previously SHRIMP-dated zircons and range from 5.90±0.35‰ to 6.29±0.34‰. These data yielded a weighted mean $\delta^{18}O$ value of 6.08±0.09‰ (2σ; MSWD 0.43). As with NIM011, the low MSWD suggests excellent uniform grouping of the data, suggestive of a single population. The median $\delta^{18}O$ for these zircons is 6.05±0.23‰. As for NIM011, Figure 13d shows a slight range in the $\delta^{18}O$ data from values within the 'normal' mantle field to just outside (>5.9‰). This may suggest mixing between a mantle-derived and heavy $\delta^{18}O$ component (see Discussion). However, the median and weighted mean values for this sample are within error of the mantle field. In addition, only two individual analyses fall outside of the mantle range (12-1, 20-1). These observations, together with the low MSWD, suggest the $\delta^{18}O$ data from SPHGEO1 constitute uniform group and that internal $\delta^{18}O$ variation is a function of zircon quality and preservation. Figure 13b demonstrates that this sample, with a MSWD of 2.2 in U-Pb space, also has the greater variability in $\delta^{18}O$. NIM011 has very low internal variability in both U-Pb and $\delta^{18}O$ space, suggesting these grains are slightly better preserved.

9. Pb isotopes

9.1. Methods

Samples of galena were analysed from the Nimbus deposit for Pb isotopes to characterize the isotopic affinity of the underlying crust and source of metals (e.g. Huston et al., 2014). Galena was hand-picked under the microscope from two samples of mineralized dacite (NBDH013_334m and NBDH035_175m) for Pb isotope analysis. Samples were dissolved and prepared using standard wet chemical techniques. Prepared filaments loaded into a Triton Thermal Ionization Mass Spectrometer (TIMS) at Curtin University, Western Australia. Wet chemical techniques, operating conditions, precision and accuracy are detailed in the Supplementary Information.

9.2. Results

Lead isotope results from Nimbus are presented in Supplementary Table 7 and plotted in Figure 14, together with published Pb isotope data from across the Eastern Goldfields. The two samples analysed have almost identical $^{206}Pb/^{204}Pb$ (13.49), $^{207}Pb/^{204}Pb$ (14.68) and $^{208}Pb/^{204}Pb$ (33.27-33.28) ratios. These values are quite close to that of pyrite from an unnamed Kambalda-type komatiitic Ni sulfide deposit analysed by McNaughton et al. (1990; $^{206}Pb/^{204}Pb=13.52$; $^{207}Pb/^{204}Pb=14.65$). Published values from galena and chalcopyrite of the ca. 2690 Ma Teutonic Bore, Jaguar and Bentley VHMS deposits have significantly lower $^{206}Pb/^{204}Pb$ (13.36-13.40), $^{207}Pb/^{204}Pb$ (14.53-14.55) and $^{208}Pb/^{204}Pb$ (33.14-33.22) ratios than those obtained from Nimbus (Vaaskoki, 1985; Browning et al. 1987; Dahl et al. 1987; McNaughton et al. 1990; Huston et al. 2014). Using the Cumming and Richards (1975) model, calculated model ages for the Nimbus and Teutonic Bore deposits are similar at 2.76 and 2.75 Ga. According to McNaughton et al. (1990), this model overestimates the ages of mineral deposits in the Eastern Goldfields by ~0.7 Ga. This is consistent with the two new SHRIMP U-Pb zircon ages from Nimbus presented here (ca. 2703 Ma), and existing U-Pb zircon constraints from Teutonic Bore (ca. 2690 Ma; Pidgeon & Wilde, 1990; Nelson, 1995). The Abitibi-Wawa model was developed for the Abitibi province of Canada (e.g., Thorpe, 1999), but it is also considered to be applicable for the Eastern Goldfields Superterrane (Huston et al., 2014). This model gives quite accurate Pb-Pb model ages of 2.70 Ga using a μ ($^{238}U/^{204}Pb$) value of 7.65 (instead of 8 used by Huston et al., 2014). Calculated μ ($^{238}U/^{204}Pb$) values from Nimbus using the Abitibi-Wawa model are 8.34, which is significantly higher than the Teutonic Bore, Jaguar and Bentley VHMS deposits (μ = ~8.06; Huston et al., 2014).

10. Discussion

10.1. Formation the Nimbus stratigraphy

The presence of peperitic upper and lower contacts for mafic rocks at Nimbus (Fig. 6i) and abundant hyaloclastite (Fig. 9j) suggests that mafic rocks most likely represented shallow invasive flows or sills into unconsolidated wet sediments (detailed in Hildrew et al., in prep). Furthermore, the presence of peperitic contacts between carbonaceous mudstones and the host dacite (e.g. Doyle, 1998) indicates that all units were broadly coeval and syn-depositional in timing (Fig. 15a). Although it is not clear whether the polymict volcanic conglomerates NE of Nimbus (which contain variably altered clasts of dacite) form part of the stratigraphic hanging-wall or footwall (see Stratigraphy), these rocks display evidence for the reworking of dacitic clasts in a high-energy environment, and their emplacement into an anoxic basin via turbidity currents (Hildrew et al. In prep). A shallow water environment (below storm wave base) is favoured based on metal associations (e.g. high Ag, Hg; see Section 10.4). Distal expressions of these turbidity currents may be represented by the thick sequences of sandstone and mudstone in drillhole BODH015. The presence of komatiites are indicative that the sequence was deposited during a period of plume magmatism - either cycle 1 or 2 of Hayman et al.(2015). Two new U-Pb zircon SHRIMP dates of 2703 ± 5 Ma and 2702 ± 4 Ma from the host dacite indicate that the local stratigraphy forms part of the Kambalda Sequence (cycle 2 of Fig. 3).

10.2. Tectonic Setting: geochemical and geological evidence

There is still considerable debate on the tectonic setting of the >2.72 Ga stratigraphy of the Eastern Goldfields Superterrane. Competing models for the formation of the Yilgarn Craton variably invoke Archean subduction, arc and/or plume magmatism, rifting and the accretion of allochtonous terranes (discussed in Czarnota et al., 2010; Barnes et al., 2012; Van Kranendonk et al., 2013; Hollis et al., 2015). Debate primarily concerns whether subduction is required to explain the evolution of the Eastern Goldfields Superterrane (EGS) and which of the various terranes and domains have a common history. While a number of workers favour both plume and subduction processes (Czarnota et al., 2010), others highlight the problem of scale as plume magmatism is expected to overwhelm subduction (Barnes et al., 2012; Van Kranendonk et al., 2013; Barnes & Van Kranendonk, 2014). In addition, there is no physical geological evidence of the existence of a subduction accretionary prism or melange zone, or of a blueschist facies metamorphic zone anywhere in the Yilgarn Craton.

Data presented here are consistent with the findings of Barnes et al. (2012), Barnes and Van Kranendonk (2014), and Hayman et al. (2015b), that plume magmatism combined with assimilation-fractional crystallization processes and magma-mixing can produce all the observed geochemical characteristics for mafic, intermediate and felsic rocks in the Eastern Goldfields. Although all mafic rocks from Nimbus plot in the nMORB to eMORB/WPB and arc-related (e.g. IAT, BABB) fields of various tectonic discrimination diagrams (Fig. 10a-b), they bear a striking resemblance to the low-Th suite of Barnes et al. (2012), suggested to represent plume head lavas, common throughout both the Kalgoorlie and Kurnalpi terranes.

Perhaps the most convincing argument is that komatiites require high degrees of partial melting only possible in a mantle plume (see Campbell & Hill, 1988). Whereas komatiitic cumulate bodies of the Kalgoorlie Terrane are interpreted as the products of high-flux komatiite volcanism focussed along the eastern margin of the Youanmi Terrane (Fig. 1), thin and sparsely distributed komatiites of the Kurnalpi terrane most likely represent flows or ponded lava lakes (Barnes et al., 2012). As the overlying Devon Consols and Paringa basalts of the Kalgoorlie Terrane (Fig. 3b) can be modelled through progressive contamination and fractionation of plume derived magma, it is logical to attribute their origins to a plume source as well (Barnes et al., 2012; Hayman et al., 2015b). The problem with using tectonic discriminations for Archaean rocks where contamination from pre-existing continental crust is common (detailed in Wyche et al., 2013; Mole et al., 2013) is highlighted in Figure 11 and discussed by Bédard et al. (2013; also Pearce, 2008). The Devon Consols and Paringa basalts parallel the trend of samples from Teutonic Bore (frequently ascribed to an island arc/backarc; see following), and in reality none may have formed above a subduction zone. As argued by Bédard et al. (2013), Archaean magmas frequently interpreted as being arc-related often do not have Th/Yb and Nb/Yb ratios that parallel the mantle array - a typical feature of Phanerozoic arcs, caused by an addition of Th to the source without changing Nb or Yb. This is highlighted by the oblique trend to the mantle array in Figure 11c caused by fractional crystallization and crustal contamination processes (Pearce, 2008; Bédard et al., 2013).

In order to explain the petrogenesis of <2.72 Ga intermediate and felsic rocks of the Kurnalpi and Kalgoorlie terranes Czarnota et al. (2010) suggested that west dipping subduction was initiated between 2715 Ma and 2690 Ma. This resulted in arc volcanism in the Kurnalpi Terrane and backarc extension in the Kalgoorlie Terrane. In addition to the above geochemical arguments against subduction (due to a lack of diagnostic criteria), the paucity of andesites at Nimbus and throughout the Kalgoorlie terrane is also difficult to reconcile if the Nimbus dacites formed in a 'continental arc' (Fig. 11c). If a backarc scenario is proposed for the Kalgoorlie Terrane, as in Czarnota et al. (2010), this is at odds with the FI affinity and strongly HREE-depleted TTG-like character of the Nimbus dacites, implying a thickened crust and deep crustal melting (see section 10.5).

10.3. Tectonic setting: isotopic evidence

Oxygen isotope data presented here represents the first of its kind from felsic volcanic rocks of the Yilgarn Craton, and hence offers a new window into the genesis of these magmas. As discussed in detail in section 8.2, $\delta^{18}O$ results from ca. 2703 Ma zircons of NIM011 and SPHGEO1 demonstrate a predominant mantle affinity. In sample NIM011 the median and weighted mean values overlap with the mantle zircon field (within error) and all individual analyses overlap with this field. In SPHGEO1, there is slightly more variation, however the median and 14 of 16 analyses still overlap with the mantle zircon field. Only the weighted mean value and two data-points (12-1, 23-1; SPHEGEO1) fall outside of the mantle range, and by a very small margin (0.01‰ and 0.05‰, respectively; Fig. 13c-d). In addition to this, despite the small amount of enrichment evident by the fact the data does not plot directly within the mantle range, all data points, medians and weighted means are below the 6.5‰ cut-off for zircons considered to have a mantle source and minor to negligible sedimentary component (Cavosie et al., 2005; Kemp et al., 2006). These data, taken together, suggest a mantle affinity for zircons from the Nimbus dacite (median of all data is 6.03±0.23‰). However, there appears to be evidence of slight enrichment in $\delta^{18}O$ as suggested by absolute median, weighted mean and individual analyses slightly above, but within error of, the mantle zircon field (Fig. 13b). This suggests mixing, homogenization (borne out by the low MSWD) between a heavy $\delta^{18}O$ source and mantle-derived material.

Some sources of heavy $\delta^{18}O$ material in geological systems are presented in Figure 13a. These are predominantly sedimentary material, altered oceanic crust/volcanics, metamorphic rocks and slab/sediment melts. Hence incorporation of one or multiple of these components could lead to the slight enrichment observed in the zircons of the Nimbus dacite. The enrichment appears to be minor, as most values for these samples overlap with the mantle-zircon field. This suggests that any additional material added was either moderately heavy, or in small volumes relative to the mantle component.

The lack of known high-grade metamorphic rocks in the area appears to preclude their involvement. The incorporation of slab and/or sediment melts is a possibility but infers a convergent margin setting (oceanic or continental arc). Whilst collated data in Figure 13a demonstrates the difficulty in using $\delta^{18}O$ values as an indicator of tectonic setting, due to overlap in signatures for various settings, these data indicate incorporation of a high $\delta^{18}O$ component via subduction is unlikely. Firstly, the data presented in Figure 13b is remarkably uniform (low MSWD), and does not demonstrate the 'trend' of data from mantle-zircon to $\delta^{18}O$>6.5‰ observed in many arc settings (Bolhar et al., 2008; Dai et al., 2011; Jiang et al., 2012; King and Valley, 2001; Lackey et al., 2006; Lackey et al., 2005; Li et al., 2012; Roberts et al., 2013; Wang et al., 2013; Zheng et al., 2012; Fig. 13b). Secondly, when the data is compared to a probability density curve of arc-zircon $\delta^{18}O$ values (Fig. 13b), and their associated median (6.8‰), the Nimbus dacite falls well below that median as well as the peak of the curve (inflexion at ca. 6.5‰). This demonstrates the majority of arc zircons have a minimum $\delta^{18}O$ >6.5‰; a component not observed in the Nimbus dacite. While these observations do not rule-out an arc origin for these magmas, this information, in conjunction with regional geology, geochemistry and geochronology, makes a subduction origin for these magmas unlikely.

As detailed above, Barnes and Van Kranendonk (2014) suggest the origin of ca. 2.7 Ga felsic volcanism at Mt Keith (Agnew-Wiluna greenstone belt; Rosengren et al., 2008) and Black Swan (Boorara Domain; Cas et al. 2013) was the product of fractionation of plume/mantle-derived tholeiitic basalts and contamination with partial melts of pre-existing continental crust. Without δ^{18}O data for >2.7 Ga Yilgarn granites/TTGs, it is difficult to assess this model using the oxygen isotopes collected here. However, based on the collated zircon δ^{18}O from Archean cratons (Figs. 13b), it would initially appear that the majority of data are too 'mantle-like', to represent the enriched component in the Nimbus dacite. Relatively rare high-Mg Archean sanukitoids displaying higher δ^{18}O, averaging 6.5±0.4‰ (Superior Province; Valley et al. 2005), offer another viable contaminant, although it should be noted that Yilgarn sanukitoids are typically <2.7 Ga (Cassidy et al., 2005; Champion and Cassidy, 2007) and not typical of the TTG compositions modelled by Barnes and Van Kranendonk (2014). As a result, the model of Barnes and Van Kranendonk (2014) may be supported by the oxygen-isotope data, but this cannot be quantitatively constrained until data for the pre-2.7 Ga δ^{18}O of the Yilgarn crust is available.

As a result, our preferred model for the slight δ^{18}O enrichment observed in the Nimbus dacite is interaction, assimilation, and homogenization of a mantle-derived magma with coeval mudstones and/or basaltic rocks, both of which would have had an enriched δ^{18}O signature as suggested by data in Figure 13a (ca. 13‰ Land and Lynch, 1996, and 17-9‰ Knauth and Lowe, 2003, respectively). Incorporation of relatively small amounts of altered basalt and/or mudstone in the dacite plumbing system, as well as at the cryptodome-mudstone interface, followed by homogenization, created a source with a uniform, but slightly enriched δ^{18}O composition dominantly within error of the mantle zircon field.

Lead isotope data presented here further implicate a mantle source and the melting of pre-existing continental crust in the genesis of most VHMS and epigenetic Au orebodies of the

Eastern Goldfields (Fig. 14). Samples analysed from Nimbus plot on a mixing trend between the Archean mantle (i.e. values closer to Teutonic Bore) and continental crust (represented by Stennet granodiorite; see McNaughton and Groves, 1996), comparable to epigenetic Au deposits of the Eastern Goldfields (McNaughton et al. 1990; 1993; Fig. 14). Galena from Nimbus is more radiogenic than the Teutonic Bore ore cluster (Teutonic Bore, Jaguar and Bentley deposits) and has a similar isotopic composition to Kambalda-type Ni sulfide deposits (McNaughton et al., 1990), which is consistent with an overall increase of a radiogenic lead component southwards within the Norseman-Wiluna Terrain (McNaughton and Groves, 1996; Fig. 14) and the position of Nimbus on the margin of the Kurnalpi rift zone (see Section 10.5).

10.4. Genesis of the Nimbus Ag-Zn deposit

Data presented here are consistent with the Nimbus Ag-Zn-(Au) deposit representing a relatively shallow-water and low-temperature VHMS deposit with epithermal characteristics. Petrographic evidence, including the replacement of dacite by early 'colloform' pyrite (e.g. Crawford, 2012) and monomict dacite breccias by Ag-Zn-Pb-(Au) rich massive sulfides, indicate that the Nimbus deposit formed sub-seafloor through the replacement of the host stratigraphy. Hydrothermal fluids were preferentially focussed through the most permeable strata (Fig. 15). Quench fragmented monomict dacite breccias were particularly susceptible, due to the breakdown and replacement of volcanic glass in the matrix (Fig. 6g), and eventually the replacement of clasts themselves (Fig. 8e). Massive Ag-Zn-Pb-(Au) mineralization is best developed where these breccias are thickest, with a complete transition of both massive Ag-Zn-Pb-(Au) mineralization and quench fragmented dacite (Fig. 8e) into a weakly mineralized (stringer sphalerite-pyrite) and coherent dacite facies (Fig. 8k). Breccia ores and stringer veins which connect lenses of massive sulfide may have acted as feeders, and are commonly marked by hydraulic fracture breccia zones, propagated by over-pressured hydrothermal fluids (cf. Cas et al., 2011). Similar preferential fluid flow is evident in the mafic rocks where coherent units are evenly altered (quartz-carbonate-chlorite; Supplementary Fig. 1h) and in hyaloclastite the matrix was the first phase to be altered and mineralized (Supplementary Fig. 1f). Contacts between mafic and felsic rocks also focussed hydrothermal fluids, which are associated with broad zones of sericite-carbonate-fuchsite-chlorite alteration (Fig. 10h). Narrow zones of intense chloritization (Fig. 9e) were most likely associated with higher-temperature fluid pathways and may have once been zones of hydrothermal hydraulic fracturing (e.g. Fig. 9i), or faults (Fig. 15).

The mineralogy of the Nimbus deposit is consistent with a low temperature (<200 ˚C) system; this includes: (i) low Cu-Au throughout most of the deposit (including only trace amounts of chalcopyrite in most lenses); (ii) the abundance of Ag-Sb-As-Pb bearing sulfosalts (drawing parallels to modern hydrothermal systems and hybrid VHMS-epithermal deposits – see following); and (iii) high Hg in sphalerite (McArthur, 2012). Alteration assemblages associated with mineralization at Nimbus are also typical of lower temperature VHMS deposits. The distal albitic alteration may have formed during diagenesis or reflect a low temperature hydrothermal alteration assemblage (Doyle, 1998). The latter often surround sericitic zones of felsic-hosted VHMS deposits (e.g. Bathurst Mining Camp, Mount Read province; Large et al., 1996; Goodfellow & McCutcheon, 2003). The primary mineral assemblage of pyrite, tetrahedrite and minor chalcopyrite indicate Nimbus was of intermediate sulfidation, although the presence of covellite, enargite (associated with chalcopyrite) and freibergite in holes NBRC202 and NBRC203 (McArthur, 2012; blue bars in Fig. 4) suggest some lenses may have been of higher sulfidation (e.g. Yeats et al., 2014).

Regarding the nature of the hydrothermal fluid involved in mineralization, the preservation of phenocrysts throughout much of the deposit, and an abundance of sericite with little chlorite, suggests ascending hydrothermal fluids were dominated by a magmatic component with minimal seawater (Doyle, 1998; Fig. 15). It is also clear that some sections of massive pyrite did not experience the Zn-Pb-Ag event (marked by a complete absence of base metal sulfides and sulfosalts). This may be indicative of some degree of compartmentalisation of the hydrothermal fluids throughout the deposit. The distribution of arsenopyrite is also patchy throughout the deposit, suggesting some mineralized lenses were effectively sealed during the introduction of As and possibly Au (as the two are broadly correlated).

A potential modern analogue for the Nimbus deposit is the Palinuro Volcanic Complex, Aeolian arc, Italy, where sub-seafloor mineralization occurs at water depths of ~650mbsl (metres below sea level; Petersen et al., 2014). In addition to the presence of Ag-Au rich massive sulfides of comparable grade to Nimbus (0.4 g/t Au & 130ppm Ag; to 925ppm Ag locally), the main low temperature phase is somewhat similar. The barite cap is cemented and was brecciated by barite-pyrite, minor chalcopyrite, tetrahedrite, trace famatinite [$Cu_3Sb_3S_4$] and rare cinnabar. A low-temperature phase of sphalerite, galena, opal-A, barite and Pb-Sb-As sulfosalts (e.g. bournonite, semseyite [$Pb_9Sb_8S_{21}$] occurred prior to a transition to very high sulfidation (marked by enargite and hypogene covellite with galena and sphalerite) and the formation of late colloform pyrite and marcasite. Similar precious metal rich VHMS deposits in Canada include the Au-Ag-Cu-Zn Eskay Creek deposit, interpreted to have formed at <200 ˚C and ~1500 mbsl from fluid inclusion evidence (see Barrett & Sherlock, 1996; Sherlock et al., 1999).

10.5. Implications for VHMS exploration in the Eastern Goldfields

Recent work on the timing, setting and style of VHMS mineralization in the Yilgarn Craton has emphasized the importance of episodic linear zones which apparently provide strong controls on the focus of mineralization (Huston et al., 2014; Hollis et al., 2015; Fig. 2). It has also given rise to an investigation of the potential for additional discoveries in similar geodynamic settings (e.g. Bore Well, Erayinia/King, Mount Gill; Fig. 1; Hollis et al., in press). Compared to other VHMS occurrences in the Yilgarn Craton, the Nimbus deposit is unusual in terms of its tectono-stratigraphic position, the geochemistry of its host sequence, its mineralogy, and alteration assemblages.

The tectono-stratigraphic position of the Nimbus deposit is unusual in two regards: (i) its position in the Kalgoorlie Terrane, where no other VHMS deposits have been discovered (discounting barren pyritic lenses), and (ii) its age. Two new U-Pb zircon SHRIMP dates of 2703 ± 5 Ma and 2702 ± 4 Ma from the host dacite indicate that the local stratigraphy forms part of the Kambalda Sequence (Fig. 3). This is further substantiated by the presence of Al-undepleted Munro-type komatiites in drillhole BODH015 and low-Th tholeiitic basalts throughout the deposit stratigraphy (Fig. 10b-d). Cr-V rich fluids that produced the fuchsite at Nimbus may have also been sourced from the alteration of komatiites deeper in the volcanic pile. The only other known VHMS deposits of this age occur in the Kurnalpi rift zone. At Anaconda (Fig. 2), historic mining mainly prior to 1908 produced 4595 t Cu from supergene mineralization above small copper–zinc sulfide lenses (Marston, 1979). Felsic tuff from Anaconda yielded an age of 2698 ± 5 Ma (Nelson, 2005), which together with the presence of interbedded komatiites at the nearby base metal Rio Tinto occurrence, suggest the sequence forms part of the 2.7 Ga plume stratigraphy of the Kurnalpi Terrane (Hollis et al., 2015). The recognition that the Nimbus deposit is associated with 2.7 Ga plume magmatism opens up new areas for VHMS exploration in the Kalgoorlie Terrane over a strike length exceeding 500 km.

The presence of FI affinity felsic rocks at Nimbus also makes it unique for a VHMS deposit in the Yilgarn Craton (reviewed in Hollis et al., 2015), which may be explained by its position near the margin of the Kurnalpi rift zone. All other significant VHMS occurrences in the Eastern Goldfields are located in the Kurnalpi rift zone and are associated with FII to FIII affinity felsic rocks, which display flat chondrite-normalized HREE profiles, slightly enriched

LREE profiles, and low ratios of Zr/Y, Th/Yb and Sc/V (Hollis et al. 2015). FIII affinity felsic rocks are normally produced by shallow crustal melting associated with crustal extension (e.g. Lesher et al., 1986; Piercey et al., 2001; Hart et al., 2004). Consequently, the elevated geothermal gradients are thought to be the main driver for hydrothermal circulation in the upper crust and the formation of VHMS mineralization. The FI character of the Nimbus dacite (Fig. 10e-f) implies deep crustal melting and the presence of garnet in the source region (Lesher et al., 1986). Consequently, it is more likely that plume magmatism provided the heat that drove the hydrothermal system.

Classification of Nimbus as a shallow water VHMS deposit with epithermal characteristics is also consistent with its position in the Kalgoorlie Terrane, near the margin of the Kurnalpi rift zone. Hybrid bimodal-felsic VHMS deposits (Piercey, 2011) typically form in more evolved and thicker crust compared to those with classic Noranda-type Cu-Zn deposits (e.g. Teutonic Bore, Jaguar, King) (Mercier-Langevin et al., 2011). Furthermore, they are often associated with subsurface phase separation (resulting in precious metal enrichment) and a strong magmatic input into the hydrothermal system (Mercier-Langevin et al., 2011; Fig. 15). This is consistent with our observations from the Nimbus deposit and μ values (see Fig. 2 caption for definition) that are significantly more radiogenic than those from the Teutonic Bore, Jaguar and Bentley VHMS deposits (Fig. 14). Comparable values to those obtained here from Nimbus occur north of Kalgoorlie along the margins of the Kurnalpi rift zone (Fig. 2c). One consequence of this is that prospectivity studies which use the geochemistry of felsic volcanic rocks to rule out potential areas for mineralization may overlook precious metal rich VHMS deposits in the Kalgoorlie Terrane, as they are more likely to be associated with FI affinity felsic rocks than those of FIII affinity.

The observation that the Nimbus stratigraphy is distinctly bimodal (basalt-dacite; Fig. 10a; Fig. 15) is also in stark contrast to VHMS deposits of the Kurnalpi rift zone. Economic mineralization at Teutonic Bore is hosted in a ca. 2690 Ma sequence which includes FII to FIII affinity felsic volcanic rocks (Fig. 10i), with ore closely associated with deep marine argillaceous metasedimentary rocks (Belford, 2010; Belford et al., 2015). A significant thickness of andesite occurs in the hanging-wall of all three deposits (i.e. Teutonic Bore, Jaguar and Bentley; Fig. 10i). Andesitic rocks are also a common part of the stratigraphy at Erayinia in the southern part of the Kurnalpi Terrane, where the King deposit (2.146 Mt at 3.47% Zn, non-compliant) occurs as two small stratiform replacive lenses in a structurally overturned volcanic–sedimentary sequence (Hollis et al. in prep). Barnes and Van Kranendonk (2014) suggested that andesites are common in the Kurnalpi Terrane away from the centre of the 2.72 Ga mantle plume, as low Th tholeiitic basalt and TTG dacite mixed in middle-upper crustal magma chambers to form a spectrum of andesitic magmas. By contrast, in the Kalgoorlie terrane, magmatism was dominated by coeval komatiite, low-Th basalt and TTG dacite (Barnes & Van Kranendonk, 2014).

The absence of significant chloritic alteration at Nimbus is unique for VHMS deposits in the Archaean Yilgarn Craton. Consequently, many classic vectors to ore such as the intensity of chloritic alteration, chlorite chemistry (e.g. Fe/Mg ratios using electron microprobe or hyperspectral data) and alteration indices (e.g. the Box Plot of Large et al. 2001; Hollis et al., In prep) will not be suitable for the discovery of Nimbus style mineralization in the Kalgoorlie Terrane, along the margin of the Kurnalpi rift zone. Instead, the recognition of intense sericite-carbonate±fuchsite alteration in FI affinity dacite, associated with substantial gains in pathfinder elements As, Sb, Cd and Tl (see Supplementary Information), would be significant.

11. Conclusions

Data presented here is consistent with the Nimbus Ag-Zn-(Au) deposit representing a shallow-water and low-temperature, intermediate sulfidation VHMS deposit. Two new U-Pb zircon SHRIMP ages of 2703 ± 5 Ma and 2702 ± 4 Ma from host dacite indicate the Nimbus deposit was coeval with plume magmatism in the Eastern Goldfields, with the local stratigraphy forming part of the Kambalda Sequence. Compared to other VHMS occurrences in the Yilgarn Craton, the Nimbus deposit is unusual in terms of its tectono-stratigraphic position, the geochemistry of its host sequence (i.e. FI-affinity felsic volcanic rocks, ocean-plateau-like low-Th basalts), mineralogy (e.g. abundance of Ag-Sb-Pb-As bearing sulfosalts, high Hg, low Cu) and quartz-carbonate-sericite dominated alteration assemblages. Classification of Nimbus as a shallow water and low temperature VHMS deposit with epithermal characteristics (i.e. a hybrid bimodal-felsic deposit) is consistent with its position near the margin of this paleo-rift zone, and more radiogenic Pb isotopic values than galena from the Teutonic Bore VHMS deposits. The recognition that the Nimbus deposit is associated with 2.7 Ga plume magmatism opens up new areas for VHMS exploration in the Eastern Goldfields Superterrane over a strike length exceeding 500 km.

Acknowledgements

This work builds on the efforts of a large number of individuals, including many company and consulting geologists who have worked on the Nimbus deposit since 1993, particularly Mark Doyle. Valery Maslennikov is thanked for insightful discussions on the geology of the Nimbus deposit. The principal author was supported by the Exploration Incentive Scheme at the Geological Survey of Western Australia, funded by the Western Australian Government Royalties for Regions Program. Steven Hollis is currently supported by the Irish Centre for Research in Applied Geosciences (iCRAG). iCRAG is funded under the Science Foundation

Ireland Research Centres Programme and is co-funded under the European Regional Development Fund. The authors acknowledge the facilities, and the scientific and technical assistance of the Australian Microscopy & Microanalysis Research Facility at the Centre for Microscopy, Characterisation & Analysis, The University of Western Australia, a facility funded by the University, State and Commonwealth Governments. Comments from Editor Randall Parrish, Pat Hayman and an anonymous reviewer greatly improved this manuscript.

References

Arndt, N. & Lesher, C.M. (2004) Komatiite. *Encyclopaedia of Geology*. Elsevier, pp260-268.

Arthur, M.A., Anderson, T.F. & Kaplan, I.R. (1983) Stable isotopes in sedimentary geology. SEPM Short Course 10, 432.

Barley, M.E., Brown, S.J.A., Krapež, B. & Kositcin, N. (2008) Physical volcanology and geochemistry of a Late Archaean volcanic arc: Kurnalpi and Gindalbie Terranes, Eastern Goldfields Superterrane, Western Australia. *Precambrian Research,* **161**, 53-76.

Barnes, S.J. (2006) Komatiite-hosted nickel sulfide deposits: Geology, geochemistry, and genesis. *Society of Economic Geology Special Publication*, **13**, 51-97.

Barnes, S.J. & Fiorentini, M.L. (2012) Komatiite magmas and sulfide nickel deposits: a comparison of variably endowed Archean terranes. *Economic Geology*, **107**, 755-780.

Barnes, S.J. & Van Kranendonk, M.J. (2014) Archean andesites in the East Yilgarn Craton, Australia: products of plume/crust interaction? *Lithos*, **6**, 80-92.

Barnes, S.J., Van Kranendonk, M.J. & Sonntag, I. (2012) Geochemistry and tectonic setting of basalts from the Eastern Goldfields Superterrane. *Australian Journal of Earth Sciences*, **59**, 707-735.

Barrett, T.J. & Sherlock, R.L. (1996) Geology, lithogeochemistry and volcanic setting of the Eskay Creek Au-Ag-Cu-Zn deposit, northwestern British Columbia. *Exploration and Mining Geology*, **5**, 339-368.

Bédard, J.H., Harris, L.B. & Thurston, P.C. (2013) The hunting of the snArc. *Precambrian Research*, **229**, 20-48.

Belford, S.M. (2010) Genetic and Chemical Characterisation of the Host Succession to the Archean Jaguar VHMS Deposit. University of Tasmania. Unpublished Ph.D. thesis.

Belford, S.M. (2011) The Nimbus deposit: notes and thoughts on what can be determined from the diamond drillcore regarding the setting and geological model. Unpublished report for MacPhersons Reward Gold Ltd. June 2011, 8pp.June 2011, 8pp.

Belford, S.M., Davidson, G.J., McPhie, J. & Large, R.R. (2015) Architecture of the Neoarchean Jaguar VHMS deposit, Western Australia: implications for prospectivity and presence of depositional breaks. *Precambrian Research*, **260**, 136-160.

Beresford, S., Stone, W.E., Cas, R., Lahaye, Y. & Jane, M. (2005) Volcanological controls on the localization of the komatiite-hosted Ni-Cu-(PGE) Coronet Deposit, Kambalda, Western Australia. *Economic Geology*, **100**, 1457-1467.

Bindeman, I. (2008) Oxygen isotopes in mantle and crustal magmas as revealed by single crystal analysis. *Reviews in Mineralogy and Geochemistry*, **69**, 445-478.

Bindeman, I.N., Fu, B., Kita, N.T. & Valley, J.W. (2008) Origin and evolution of silicic magmatism at Yellowstone based on ion microprobe analysis of isotopically zoned zircons. *Journal of Petrology*, **49**, 163-193.

Bindeman, I.N. & Valley, J.W. (2000) Formation of low-$\delta^{18}O$ rhyolites after caldera collapse at Yellowstone, Wyoming, USA. *Geology*, **28**, 719-722.

Bindeman, I.N. & Valley, J.W. (2001) Low-$\delta^{18}O$ rhyolites from Yellowstone: Magmatic evolution based on analyses of zircons and individual phenocrysts. *Journal of Petrology*, **42**, 1491-1517.

Bindeman, I.N. & Valley, J.W. (2002) Oxygen isotope study of the Long Valley magma system, California: isotope thermometry and convection in large silicic magma bodies. *Contributions to Mineralogy and Petrology*, **144**, 185-205.

Bindeman, I.N. & Valley, J.W. (2003) Rapid generation of both high-and low-$\delta^{18}O$, large-volume silicic magmas at the Timber Mountain/Oasis Valley caldera complex, Nevada. *Geological Society of America Bulletin*, **115**, 581-595.

Black, L.P., Kamo, S.L., Allen, C.M., Davis, D.W., Aleinikoff, J.N., Valley, J.W., Mundil, R., Campbell, I.H., Korsch, R.J., Williams, I.S., Foudoulis, C. (2004) Improved $^{206}Pb/^{238}U$ microprobe geochronology by the monitoring of a trace-element-related matrix effect; SHRIMP, ID–TIMS, ELA–ICP–MS and oxygen isotope documentation for a series of zircon standards. *Chemical Geology*, **205**, 115-140.

Black, L.P., Kamo, S.L., Allen, C.M., Aleinikoff, J.N., Davis, D.W., Korsch, R.J. & Foudoulis, C. (2003) TEMORA 1: a new zircon standard for Phanerozoic U–Pb geochronology. *Chemical Geology*, **200**, 155-170.

Bolhar, R., Weaver, S., Whitehouse, M., Palin, J., Woodhead, J. & Cole, J. (2008) Sources and evolution of arc magmas inferred from coupled O and Hf isotope systematics of plutonic zircons from the Cretaceous Separation Point Suite (New Zealand). *Earth and Planetary Science Letters*, **268**, 312-324.

Brown, S.J.A., Barley, M.E., Krapež, B. & Cas, R.A.F. (2002) The Late Archaean Melita Complex, Eastern Goldfields, Western Australia: shallow submarine bimodal volcanism in a rifted arc environment. *Journal of Volcanology and Geothermal Research*, **115**, 303-327.

Browning, P., Groves, D.I., Blockley, J.G. & Rosman, K.J.R. (1987) Lead isotope constraints on the age and source of gold mineralization in the Archean Yilgarn Block, Western Australia. *Economic Geology*, **82**, 971-986.

Cabanis, B. & Lecolle, M. (1989) Le diagramme La/10-Y/15-Nb/8; un outil pour la discrimination des series volcaniques et la mise en evidence des processus de melange et/ou de contamination crustale. The La/10-Y/15-Nb-8 diagram; a tool for distinguishing volcanic series and discovering crustal mixing and/or contamination. Comptes Rendus de l'Academie des Sciences, Serie 2, Mecanique, Physique, Chimie, Sciences de l;Univers, Sciences de la Terre, 309, 2023-2029.

Campbell, I.H. & Hill, R.I. (1988) A 2-stage model for the formation of the granite-greenstone terrains of the Kalgoorlie-Norseman area, Western Australia. *Earth and Planetary Science Letters*, **90**, 11-25.

Cas, R.A.F., Giordano, G, Balsamo, F. Esposito, A. & Lo Mastro, S. (2011). Hydrothermal breccia textures and processes: Lisca Bianca Islet, Panarea Volcano, Eolian Islands, Italy. Economic Geology, 106, 437-450.

Cas, R.A.F., Marks, K., Perazzo, S., Beresford, S., Trofimovs, J. & Rosengren, N. (2013). Were intercalated komatiites and dacites at the Black Swan nickel sulfide mine, Yilgarn Craton, Western Australia emplaced as lavas or sills? The significance of breccia textures and contact relationships. Precambrian Research, 229, 133-149. doi:10.1016/j.precamres.2011.10.001

Cassidy, K.F., Champion, D.C. & Huston, D.L. (2005) Crustal evolution constraints on the metallogeny of the Yilgarn Craton. In: Mao, J. & Bierlein, F.P. (Eds.), Mineral Deposit Research: Meeting the Global Challenge: Proceedings of the Eight Biennia SGA Meeting, Beijing, China, 2005, Berlin/Heidelberg, Springer, pp. 901-904.

Cassidy, K.F., Champion, D.C., Krapež, B., Barley, M.E., Brown, S.J.A., Blewett, R.S., Groenewald, P.B. & Tyler, I.M. (2006) A revised geological framework for the Yilgarn Craton, Western Australia. Western Australia Geological Survey, Record 2006/8: 8p.

Cavosie, A., Valley, J. & Wilde, S. (2005) Magmatic $\delta^{18}O$ in 4400–3900 Ma detrital zircons: a record of the alteration and recycling of crust in the Early Archean. *Earth and Planetary Science Letters*, **235**, 663-681.

Cavosie, A.J., Kita, N.T. & Valley, J.W. (2009) Primitive oxygen-isotope ratio recorded in magmatic zircon from the Mid-Atlantic Ridge. *American Mineralogist*, **94**, 926-934.

Champion, D.C. & Cassidy, K.F. (2007) An overview of the Yilgarn Craton and its crustal evolution, in: Bierlein, F.P., C.M., K.-R. (Eds.), Proceedings of Geoconferences (WA) Inc. Kalgoorlie '07 Conference. Geoscience Australia Record 2007/14, Kalgoorlie, Western Australia, pp. 8-13.

Chen, L., Zhao, Z.-F. & Zheng, Y.-F. (2014) Origin of andesitic rocks: geochemical constraints from Mesozoic volcanics in the Luzong basin, South China. *Lithos*, **190**, 220-239.

Crawford, A.J. (2012) Petrographic report. 17 Rocks from the Nimbus Project, Western Australia. Unpublished report for MacPhersons Resources Ltd. 17/4/2012, pp93.

Cumming, G.L. & Richards, J.R. (1975) Ore lead isotope ratios in a continuously changing Earth. *Earth and Planetary Science Letters*, **28**, 155-171.

Czarnota, K., Champion, D.C., Goscombe, B., Blewett, R.S., Cassidy, K.F., Henson, P.A. & Groenewald, P.B. (2010) Geodynamics of the eastern Yilgarn Craton. *Precambrian Research*, **183**, 175-202.

Dahl, N., McNaughton, N.J. & Groves, D.I. (1987) A lead-isotope study of sulphides associated with gold mineralization in selected gold deposits from the Eastern Goldfields of Western Australia. In: Ho, S.E. & Groves, D.I. (Eds.) *Recent Advances in Understanding Precambrian Gold Deposits.* Geology Department & University Extension, University of Western Australia, Publication No. 11, 189-201.

Dai, L.-Q., Zhao, Z.-F., Zheng, Y.-F., Li, Q., Yang, Y. & Dai, M. (2011) Zircon Hf–O isotope evidence for crust–mantle interaction during continental deep subduction. *Earth and Planetary Science Letters*, **308**, 229-244.

Doyle, M, 1998. Evaluation of genetic links between mineralisation, alteration and volcanism at Nimbus prospect, Western Australia. UNITAS Consulting, University of Tasmania. November, 1998. Unpublished report.

Duuring, P., Hassan, L., Zelic, M. & Gessner, K. (2016) Geochemical and spectral footprint of metamorphosed and deformed VMS-style mineralization in the Quinns district, Yilgarn Craton, Western Australia. *Economic Geology*, 111, 1411-1438.

Eiler, J.M. (2001) Oxygen isotope variations of basaltic lavas and upper mantle rocks. *Reviews in Mineralogy and geochemistry*, **43**, 319-364.

Ferguson, K.M. (1999) Lead, zinc and silver deposits of Western Australia. Western Australia Geological Survey, Mineral Resources Bulletin 15, 314pp.

Fiorentini, M.L., Beresford, S.W., Rosengren, N., Barley, M.E. & McCuaig, T.C. (2010) Contrasting komatiite belts, associated Ni-Cu-(PGE) deposit styles and assimilation histories. *Australian Journal of Earth Science*, **57**, 543–566.

Franklin, J.M., Gibson, H.L., Galley, A.G. & Jonasson, I.R. (2005) Volcanogenic masisve sulfide deposits. In: Hedenquist, J.W., Thompson, J.F.H., Goldfarb, R.J. & Richards, J.P. (eds.). Economic Geology 100th Anniversary Volume, Society of Economic Geologists, 523-560.

Gilliam, C.E. & Valley, J.W. (1997) Low δ^{18}O magma, Isle of Skye, Scotland: evidence from zircons. *Geochimica et Cosmochimica Acta*, **61**, 4975-4981.

Goodfellow, W.D. & McCutcheon, S.R. (2003) Geologic and genetic attributes of volcanic sediment-hosted massive sulfide deposits of the Bathurst mining camp, northern New Brunswick – a synthesis. *Economic Geology Monographs*, **11**, 245-301.

Gregory, R.T. & Taylor, H.P. (1981) An oxygen isotope profile in a section of Cretaceous oceanic crust, Samail Ophiolite, Oman: Evidence for δ^{18}O buffering of the oceans by deep (> 5 km) seawater-hydrothermal circulation at mid-ocean ridges. *Journal of Geophysical Research: Solid Earth*, **86**, 2737-2755.

Guilliamse, J.N. (2014) Assessing the potential for volcanic-hosted massive sulfide mineralization at Weld Range, using Golden Grove for comparison. Geological Survey of Western Australia, Report, 141. 61pp.

Hallberg, J.A. & Thompson, J.F.H. (1985) Geologic Setting of the Teutonic Bore, Massive Sulfide Deposit, Archean Yilgarn Block, Western Australia. *Economic Geology*, **80**, 1953-1964.

Hart, T.R., Gibson, H.L. & Lesher, C.M. (2004) Trace element geochemistry and petrogenesis of felsic volcanic rocks associated with volcanogenic massive Cu-Zn-Pb sulfide deposits. *Economic Geology*, **99**, 1003-1013.

Hassan, L.Y. (2014) The Yuinmery volcanogenic massive sulfide prospects: mineralization, metasomatism and geology. Geological Survey of Western Australia Report 131, 65pp.

Hastie, A.R., Kerr, A.C., Pearce, J.A. & Mitchell, S.F. (2007) Classification of altered volcanic island arc rocks using immobile trace elements: development of the Th-Co discrimination diagram. *Journal of Petrology*, **48**, 2341-2357.

Hayman, P.C., Hull, S.E., Cas, R.A.F., Summerhayes, E., Amelin, Y., Ivanic, T. & Price, D. (2015a) A new period of volcanogenic massive sulphide formation in the Yilgarn: a volcanological study of the ca 2.76 Ma Hollandaire VMS deposit, Yilgarn Craton, Western Australia. *Australian Journal of Earth Sciences*, **62**, 189-210.

Hayman, P.C., Thébaud, N., Pawley, M.J., Barnes, S.J., Cas, R.A.F., Amelin, Y., Sapkota, J., Squire, R.J., Campbell, I.H. & Pegg. I. (2015b) Evolution of a ~2.7 Ga large igneous province: a volcanological, geochemical and geochronological study of the Agnew Greenstone Belt, and new regional correlations for the Kalgoorlie Terrane (Yilgarn Craton, Western Australia). *Precambrian Research*, **270**, 334-368.

Heilimo, E., Halla, J., Andersen, T. & Huhma, H. (2013) Neoarchean crustal recycling and mantle metasomatism: Hf–Nd–Pb–O isotope evidence from sanukitoids of the Fennoscandian shield. *Precambrian Research*, **228**, 250-266.

Henderson, I., Goodz, M. & Vearncombe, J. (2012) Nimbus: Fault-hosted Ag-Zn-Pb-Au Mineralisation near Kalgoorlie, Western Australia. AIG Structural Geology and Resources 2012, 89-92.

Hildrew, C.L. (2015) Understanding the nature of host rock succession to the Archaean Nimbus Ag-Zn-Pb-Au deposit, WA. Unpublished MSc thesis. School of Physical Sciences, University of Tasmania.

Hoefs, J. (2008) Stable isotope geochemistry. Springer Science & Business Media.

Hollis, S.P., Yeats, C.J., Wyche, S., Barnes, S.J., Ivanic, T.J., Belford, S.M., Davidson, G.J., Roache, A.J. & Wingate, M.T.D. (2015) A review of volcanic-hosted massive sulfide (VHMS) mineralization in the Archaean Yilgarn Craton, Western Australia: Tectonic, stratigraphic and geochemical associations. *Precambrian Research*, **260**, 113-135.

Hollis, S.P., Yeats, C.J., Wyche, S., Barnes, S.J. & Ivanic, T. (In Press) VHMS mineralization in the Yilgarn Craton, Western Australia: a review of known deposits and prospectivity analysis of felsic volcanic rocks. Geological Survey of Western Australia, Report.

Huston, D.L., Champion, D.C. & Cassidy, K.F. (2014) Tectonic controls on the endowment of Neoarchean cratons in volcanic-hosted massive sulfide deposits: evidence from lead and neodymium isotopes. *Economic Geology*, **109**, 11–26.

Ivanic, T.J., Wingate, M.T.D., Kirkland, C.L., Van Kranendonk, M.J. & Wyche, S. (2010). Age and significance of voluminous mafic-ultramafic magmatic events in the Murchison Domain, Yilgarn Craton. *Australian Journal of Earth Sciences*, **57**, 597-614.

Ivanic, T.J., Van Kranendonk, M.J., Kirkland, C.L., Wyche, S., Wingate, M.T.D. & Belousova, E.A. (2012) Zircon Lu-Hf isotopes and granite geochemistry of the Murchison Domain of the Yilgarn Craton: evidence for reworking of Eoarchean crust during the Meso-Neoarchean. *Lithos*, **148**, 112-127.

Jenner, G.A. (1996) Trace element geochemistry of igneous rocks: geochemical nomenclature and analytical geochemistry. In: Wyman, D.A. (Ed.) *Trace Element Geochemistry of Volcanic Rocks: Applications for Massive Sulfide Exploration*. Geological Association of Canada, Short Course Notes 12, 51-77.

Jiang, N., Chen, J., Guo, J. & Chang, G. (2012). In situ zircon U–Pb, oxygen and hafnium isotopic compositions of Jurassic granites from the North China craton: evidence for Triassic subduction of continental crust and subsequent metamorphism-related ^{18}O depletion. *Lithos*, **142**, 84-94.

Kemp, A.I.S., Hawkesworth, C.J., Paterson, B.A. & Kinny, P.D. (2006) Episodic growth of the Gondwana supercontinent from hafnium and oxygen isotopes in zircon. *Nature*, **439**, 580-583.

King, E., Valley, J. & Davis, D. (2000) Oxygen isotope evolution of volcanic rocks at the Sturgeon Lake volcanic complex, Ontario. *Canadian Journal of Earth Sciences*, **37**, 39-50.

King, E.M. & Valley, J.W. (2001) The source, magmatic contamination, and alteration of the Idaho batholith. *Contributions to Mineralogy and Petrology*, **142**, 72-88.

King, E.M., Valley, J.W., Davis, D.W. & Edwards, G.R. (1998). Oxygen isotope ratios of Archean plutonic zircons from granite–greenstone belts of the Superior Province: indicator of magmatic source. *Precambrian Research*, **92**, 365-387.

Kita, N.T., Ushikubo, T., Fu, B. & Valley, J.W. (2009) High precision SIMS oxygen isotope analysis and the effect of sample topography. *Chemical Geology*, **264**, 43-57.

Kitajima, K., Ushikubo, T., Kita, N.T., Maruyama, S. & Valley, J.W. (2012) Relative retention of trace element and oxygen isotope ratios in zircon from Archean rhyolite, Panorama Formation, North Pole Dome, Pilbara Craton, Western Australia. *Chemical Geology*, **332**, 102-115.

Knauth, L.P. & Lowe, D.R. (2003) High Archean climatic temperature inferred from oxygen isotope geochemistry of cherts in the 3.5 Ga Swaziland Supergroup, South Africa. *Geological Society of America Bulletin*, **115**, 566-580.

Krapež, B. & Hand, J.L. (2008). Late Archaean deep-marine volcaniclastic sedimentation in an arc-related basin: the Kalgoorlie Sequence of the Eastern Goldfields Superterrane, Yilgarn Craton, Western Australia. *Precambrian Research,* **161**, 89-113.

Lackey, J.S., Valley, J.W. & Hinke, H.J. (2006) Deciphering the source and contamination history of peraluminous magmas using $\delta^{18}O$ of accessory minerals: examples from garnet-bearing plutons of the Sierra Nevada batholith. *Contributions to Mineralogy and Petrology*, **151**, 20-44.

Lackey, J.S., Valley, J.W. & Saleeby, J.B. (2005) Supracrustal input to magmas in the deep crust of Sierra Nevada batholith: evidence from high-$\delta^{18}O$ zircon. *Earth and Planetary Science Letters*, **235**, 315-330.

Land, L.S. & Lynch, F.L., 1996. $\delta^{18}O$ values of mudrocks: more evidence for an ^{18}O-buffered ocean. *Geochimica et Cosmochimica Acta*, **60**, 3347-3352.

Large, R.R., Doyle, M.G., Raymond, O.L., Cooke, D.R., Jones, A.T. & Heasman, L. (1996) Evaluation of the role of Cambrian granites in the genesis of world-class VHMS deposits in Tasmania. *Ore Geology Reviews*, **10**, 215-30.

Large, R.R., Gemmell, J.B. & Paulick H. (2011) The Alteration Box Plot: a simple approach to understanding the relationship between alteration mineralogy and lithogeochemistry associated with volcanic-hosted massive sulfide deposits. *Economic Geology*, **96**, 957-971.

Lesher, C.M., Goodwin, A.M., Campbell, I.H. & Gorton, M.P. (1986) Trace-element geochemistry of ore-associated and barren, felsic metavolcanic rocks in the Superior province, Canada. *Canadian Journal of Earth Sciences*, **23**, 222-237.

Li, X.-H., Li, W.-X., Li, Q.-L., Wang, X.-C., Liu, Y. & Yang, Y.-H. (2010) Petrogenesis and tectonic significance of the ~ 850 Ma Gangbian alkaline complex in South China: evidence from in situ zircon U–Pb dating, Hf–O isotopes and whole-rock geochemistry. *Lithos*, **114**, 1-15.

Li, X.-H., Li, Z.-X., He, B., Li, W.-X., Li, Q.-L., Gao, Y. & Wang, X.-C. (2012) The Early Permian active continental margin and crustal growth of the Cathaysia Block: in situ U–Pb, Lu–Hf and O isotope analyses of detrital zircons. *Chemical Geology*, **328**, 195-207.

Liu, J. & Zhang, L. (2013) Neoproterozoic low to negative $\delta^{18}O$ volcanic and intrusive rocks in the Qinling Mountains and their geological significance. *Precambrian Research*, **230**, 138-167.

Marjoribanks, R. (2012) Nimbus silver zinc mineralisation, Western Australia – observations, interpretations and comments. A report prepared for MacPhersons Resources Limited. MacPhersons Report No 1. 11th July 2012, 30pp.

Marston, R.J. (1979). Copper Mineralization in Western Australia. Geological Survey of Western Australia. Mineral Resources Bulletin 13, 208pp.

McArthur, G.J. (2006) Nimbus sulphide composite test work mineralogy. September 2006. Report for MacPhersons Reward Gold Ltd.

McArthur, G.J. (2012) Nimbus prospect - mineral residence of silver. December 2012. Report for MacPhersons Resources Ltd.

McNaugton, N.J. & Groves, D.I. (1996) A review of Pb-isotope constraints on the genesis of lode gold deposits in the Yilgarn Craton, Western Australia. *Journal of the Royal Society of Western Australia*, **79**, 123-129.

McNaughton, N.J., Cassidy, K.F., Groves, D.I. & Perring, C.S. (1990) Timing of mineralization. In: Ho, S.E., Groves, D.I. & Bennett, J.M. (eds). Gold deposits of the Archaean Yilgarn block, Western Australia: nature, genesis and exploration guides. Key centre for Teaching and Research in Strategic Mineral Deposits. Department of Geology, The University of Western Australia. Publication No. 20, 221-224.

Mercier-Langevin, P., Hannington, M.D., Dubé. B. & Bécu, V. (2011) The gold content of volcanogenic massive sulfide deposits. *Mineralium Deposita,* **46**, 509-539.

Mole, D.R., Fiorentini, M.L., Cassidy, K.F., Kirkland, C.L., Thébaud, N., McCuaig, T.C., Doublier, M.P., Duuring, P., Romano, S., Maas, R., Belousova, E., Barnes, S.J. & Miller, J.M. (2013) Crustal evolution, intra-cratonic architecture and the metallogeny of an Archaean craton. In: Jenkin, G.R.T., Lusty, P.A.J., McDonald, I., Smith, M.P., Boyce, A.J. & Wilkinson, J.J. (Eds.), *Ore Deposits in an Evolving Earth*. Geological Society of London Special Publication, **393**. DOI: 10.1144/SP393.8

Mole, D.R., Fiorentini, M.L., Thebaud, N., Cassify, K.F., McCuaig, T.C., Kirkland, C.L., Romano, S.S., Doublier, M.P., Belousova, E.A., Barnes, S.J. & Miller, J. (2014) Archean komatiite volcanism controlled by the evolution of early continents. *PNAS*, **111**, 10083-10088.

Monani, S. & Valley, J.W. (2001) Oxygen isotope ratios of zircon: magma genesis of low $\delta^{18}O$ granites from the British Tertiary Igneous Province, western Scotland. *Earth and Planetary Science Letters*, **184**, 377-392.

Muehlenbachs, K. (1998) The oxygen isotopic composition of the oceans, sediments and the seafloor. *Chemical Geology*, **145**, 263-273.

Mulholland, I.R., Hay, I.P., Ion, J.C., Greenaway, A.L., & Cowden, A. (1998) Nimbus Silver-Zinc Deposit. In: Berkman, D.A. & Mackenzie, D.H. (Eds.), *Geology of Australian and Papua New Guinean Mineral Deposits*. The Australian Institute of Mining and Metallurgy, Monograph **22**, 273-278.

Nasdala, L., Hofmeister, W., Norberg, N., Martinson, J.M., Corfu, F., Dörr, W., Kamo, S.L., Kennedy, A.K., Kronz, A. & Reiners, P.W. (2008) Zircon M257-a Homogeneous Natural Reference Material for the Ion Microprobe U-Pb Analysis of Zircon. *Geostandards and Geoanalytical Research*, **32**, 247-265.

Nelson, D.R. (1995) 112159: porphyritic dacite, Royal Arthur; Geochronology dataset 488, Compilation of geochronology data, June 2006 update. Western Australia Geological Society.

Pawley, M.J., Wingate, M.T.D., Kirkland, C.L., Wyche, S., Hall, C.E., Romano, S.S. & Doublier, P. (2012) Adding pieces to the puzzle: episodic crustal growth and a new terrane in the northeast Yilgarn Craton, Western Australia. *Australian Journal of Earth Sciences*, **59**, 603-623.

Pearce, J.A. (1996) A user's guide to basalt discrimination diagrams. In: Wyman, D.A. (Ed.), *Trace Element Geochemistry of Volcanic Rocks: Applications for Massive Sulfide Exploration.* Geological Association of Canada, Short Course Notes 12, 79-113.

Pearce, J.A. (2008) Geochemical fingerprinting of oceanic basalts with applications to ophiolite classification and the search for Archean oceanic crust. Lithos, 100, 14-48.

Pearce, J.A. (2014) Immobile element fingerprinting of ophiolites. *Elements*, **10**, 101-108.

Pearce, J.A. & Cann, J.R. (1973) Tectonic setting of basic volcanic rocks determined using trace element analyses. *Earth and Planetary Science Letters*, **19**, 290-300.

Peck, W.H., Valley, J.W., Wilde, S.A. & Graham, C.M. (2001) Oxygen isotope ratios and rare earth elements in 3.3 to 4.4 Ga zircons: Ion microprobe evidence for high $\delta^{18}O$ continental crust and oceans in the Early Archean. *Geochimica et Cosmochimica Acta*, **65**, 4215-4229.

Perry Jr, E. & Lefticariu, L. (2003) Formation and geochemistry of Precambrian cherts. *Treatise on geochemistry*, **7**, 407.

Pidgeon, R.T. & Wilde, S.A. (1990). Distribution of 3.0 Ga and 2.7 Ga volcanic episodes in the Yilgarn Craton of Western Australia. *Precambrian Research,* **48**, 309-325.

Piercey, S.J. (2011) The setting, style, and role of magmatism in the formation of volcanogenic massive sulphide deposits. *Mineralium Deposita*, **46**, 449-471.

Piercey, S.J., Paradis, S., Murphy, D.C. & Mortensen, J.K. (2001) Geochemistry and paleotectonic setting of felsic volcanic rocks in the Finlayson Lake, volcanic-hosted massive sulfide district, Yukon, Canada. *Economic Geology*, **96**, 1877-1905.

Powell, P. (1999) Nimbus Scoping Study. An examination of a Silver Oxide Project. Unpublished Report for Archaean Gold NL, 149pp.

Richards J.R. (1983) Lead isotopes as indicators of old stable craton in Western Australia. *Geochemical Journal*, **17**, 241-246.

Roberts, N.M., Slagstad, T., Parrish, R.R., Norry, M.J., Marker, M. & Horstwood, M.S. (2013) Sedimentary recycling in arc magmas: geochemical and U–Pb–Hf–O constraints on the Mesoproterozoic Suldal Arc, SW Norway. *Contributions to Mineralogy and Petrology*, **165**, 507-523.

Rosengren, N.M., Cas, R.A.F., Beresford, S.W. & Palich, B.M. (2008). Reconstruction of an extensive Archaean dacitic submarine volcanic complex associated with the komatiite hosted Mt Keith nickel deposit, Agnew-Wiluna Greenstone belt, Yilgarn Craton, Western Australia. *Precambrian Research*, **161**, 34-52.

Sarbas, B. & Nohl, U. (2008) The GEOROC database as part of a growing geoinformatics network. Geoinformatics.

Schandl, E.S. & Gorton, M.P. (2002) Application of high field strength elements to discriminate tectonic settings in VMS environments. Economic Geology, 97, 629-642.

Sharpe, R. & Gemmell, J.B. (2002) The Archean Cu-Zn magnetite-rich Gossan Hill volcanic-hosted massive sulphide deposit, Western Australia: genesis of a multistage hydrothermal system. *Economic Geology*, **97**, 517-539.

Sharp, Z. (2007) Principles of stable isotope geochemistry. Pearson Education Upper Saddle River, NJ.

Sherlock, R.L., Roth, T., Spooner, E.T.C. & Bray, C.J. (1999) Origin of the Eskay Creek precious metal-rich volcanogenic massive sulfide deposit: fluid inclusion and stable isotope evidence. *Economic Geology*, **94**, 803-824.

Shields, G. & Veizer, J. (2002) Precambrian marine carbonate isotope database: Version 1.1. *Geochemistry, Geophysics, Geosystems*, **3**(6), 10.1029/2001GC000266, 2002.

Siebel, W., Schmitt, A., Kiemele, E., Danišík, M. & Aydin, F. (2011) Acigöl rhyolite field, central Anatolia (part II): geochemical and isotopic (Sr–Nd–Pb, $\delta^{18}O$) constraints on volcanism involving two high-silica rhyolite suites. *Contributions to Mineralogy and Petrology*, **162**, 1233-1247.

Spencer, C.J., Cawood, P.A., Hawkesworth, C.J., Raub, T.D., Prave, A.R. & Roberts, N.M. (2014a). Proterozoic onset of crustal reworking and collisional tectonics: Reappraisal of the zircon oxygen isotope record. *Geology*, **42**, 451-454.

Spencer, C.J., Roberts, N.M., Cawood, P.A., Hawkesworth, C.J., Prave, A.R., Antonini, A.S. & Horstwood, M.S., (2014b) Intermontane basins and bimodal volcanism at the onset of the Sveconorwegian Orogeny, southern Norway. *Precambrian Research*, **252**, 107-118.

Squire, R.J., Allen, C.M., Cas, R.A.F., Campbell, I.H., Blewett, R.S. & Enchain, A.A. (2010) Two cycles of voluminous pyroclastic volcanism and sedimentation related to episodic granite emplacement during the late Archean: Eastern Yilgarn Craton, Western Australia. *Precambrian Research*, **183**, 251-274.

Stacey, J.S. & Kramers, J.D. (1975) Approximation of terrestrial lead isotope evolution by a two-stage model. *Earth and Planetary Science Letters*, **26**, 207-221.

Stern, R.A. (2001) A new isotopic and trace-element standard for the ion microprobe: preliminary thermal ionization mass spectrometry (TIMS) U-Pb and electron microprobe data. *Geological Survey of Canada Current Research*, 2001-F1.

Stern, R.A. & Ickert, R.B. (2010) Zircon oxygen isotopes by SIMS: Performance evaluation of the Canadian IMS1280, Goldschmidt 2010. Cambridge, Knoxville, Tennessee, p. A993.

Stern, R.A., Bodorkos, S., Kamo, S.L., Hickman, A.H. & Corfu, F. (2009) Measurement of SIMS instrumental mass fractionation of Pb isotopes during zircon dating. *Geostandards and Geoanalytical Research*, **33**, 145-168.

Su, B.-X., Qin, K.-Z., Sakyi, P.A., Li, X.-H., Yang, Y.-H., Sun, H., Tang, D.-M., Liu, P.-P., Xiao, Q.-H. & Malaviarachchi, S.P. (2011) U–Pb ages and Hf–O isotopes of zircons from Late Paleozoic mafic–ultramafic units in the southern Central Asian Orogenic Belt: tectonic implications and evidence for an Early-Permian mantle plume. *Gondwana Research*, **20**, 516-531.

Sverjensky, D.A. (1984) Europium redox equilibria in aqueous solution. *Earth and Planetary Science Letters*, **67**, 70-78.

Swager, C.P. (1997) Tectono-stratigraphy of the late Archaean greenstone terranes in the southern Eastern Goldfields, Western Australia. *Precambrian Research*, **83**, 11-42.

Tichomirowa, M., Whitehouse, M., Gerdes, A., Götze, J., Schulz, B. & Belyatsky, B. (2013) Different zircon recrystallization types in carbonatites caused by magma mixing: Evidence from U–Pb dating, trace element and isotope composition (Hf and O) of zircons from two Precambrian carbonatites from Fennoscandia. *Chemical Geology*, **353**, 173-198.

Townend, R. (1996) Unpublished report for Archaean Gold NL. File 25.04.10.

Trofimovs, J., Davis, B.K. & Cas, R.A.F. (2004) Contemporaneous ultramafic and felsic magmatism in the Archaean Boorara Domain, Eastern Goldfields, Western Australia, and its implications. *Precambrian Research*, **131**, 283-304.

Trofimovs, J., Davis, B.K., Cas, R.A.F., Barley, M.E. & Tripp, G.I. (2006) Reconstructing the event stratigraphy from the complex structural – stratigraphic architecture of an Archaean volcanic – intrusive – sedimentary succession: the Boorara Domain, Eastern Goldfields Superterrane, Western Australia. *Australian Journal of Earth Sciences*, **53**, 303-327.

Upton, B., Hinton, R., Aspen, P., Finch, A. & Valley, J. (1999) Megacrysts and associated xenoliths: evidence for migration of geochemically enriched melts in the upper mantle beneath Scotland. *Journal of Petrology*, **40**, 935-956.

Vaasjoki, M. (1985) The Teutonic Bore deposit, Western Australia: a lead isotope study of an ore and its gossan. *Mineralium Deposita*, **20**, 266-270.

Valley, J., Lackey, J., Cavosie, A., Clechenko, C., Spicuzza, M., Basei, M., Bindeman, I., Ferreira, V., Sial, A. & King, E. (2005) 4.4 billion years of crustal maturation: oxygen isotope ratios of magmatic zircon. *Contributions to Mineralogy and Petrology*, **150**, 561-580.

Van Kranendonk, M.J., Ivanic, T.J., Wingate, M.T.D., Kirkland, C.L. & Wyche, S. (2013). Long-lived, autochthonous development of the Archean Murchison Domain, and implications for Yilgarn Craton tectonics. *Precambrian Research*, **229**, 49-92.

Wang, F., Liu, S.-A., Li, S. & He, Y. (2013) Contrasting zircon Hf–O isotopes and trace elements between ore-bearing and ore-barren adakitic rocks in central-eastern China: implications for genetic relation to Cu–Au mineralization. *Lithos*, **156**, 97-111.

Wyche, S., Pawley, M.J., Chen, S.F., Ivanic, T.J., Zibra, I., Van Kranendonk, M.J., Spaggiari, C.V. & Wingate, M.T.D. (2013) Geology of the northern Yilgarn Craton. In: Wyche, S., Ivanic, T.J., Zibra, I. (Eds.) *Youanmi and southern*

Carnarvon seismic and magnetotelluric (MT) workshop. Geological Survey of Western Australia. Record 2013/6, pp. 31-60.

Yeats, C.J. (2007) VHMS mineral systems in the Yilgarn – characteristics and exploration potential. In: Bierlein, F.P. (Ed.) *Proceedings of Geoconferences (WA) Inc. Kalgoorlie 07 Conference*, 65–69.

Yeats, C.J. & Groves, D.I. (1998) The Archaean Mount Gibson gold deposits, Yilgarn Craton, Western Australia: products of combined synvolcanic and syntectonic alteration and mineralisation. *Ore Geology Reviews*, **13**, 103-129.

Yeats, C.J., Parr, J.M., Binns, R.A., Gemmell, J.B., Scott, S.D. (2014) The SuSu Knolls hydrothermal field, Eastern Manus Basin, Papua New Guinea: an active submarine high-sulfidation copper-gold system. *Economic Geology*, **109**, 2207-2226.

Zheng, Y.-C., Hou, Z.-Q., Li, Q.-Y., Sun, Q.-Z., Liang, W., Fu, Q., Li, W. & Huang, K.-X. (2012) Origin of Late Oligocene adakitic intrusives in the southeastern Lhasa terrane: evidence from in situ zircon U–Pb dating, Hf–O isotopes, and whole-rock geochemistry. *Lithos*, **148**, 296-311.

Zheng, Y.-F., Wu, R.-X., Wu, Y.-B., Zhang, S.-B., Yuan, H. & Wu, F.-Y. (2008) Rift melting of juvenile arc-derived crust: geochemical evidence from Neoproterozoic volcanic and granitic rocks in the Jiangnan Orogen, South China. *Precambrian Research*, **163**, 351-383

List of Figures

Figure 1. Major subdivisions of the Yilgarn Craton, Western Australia, showing the distribution of greenstone belts and base metal occurrences (excluding those associated with Ni sulfide mineralization) (after Hollis et al., 2015). Significant VHMS resources, greenstone belts (green) and base metal occurrences discussed in the text are labelled. *Domains:* B, Boorara; C, Coolgardie; O, Ora Banda; G, Gindalbie. The box shows the location of Figure 2. GB, greenstone belt; MB, metamorphic belt.

Figure 2. Regional Nd and Pb isotope variations of the Yilgarn Craton. (a) Nd-depleted mantle model (Nd_{DM}) age map of the northern Yilgarn Craton (after Champion & Cassidy, 2007; Czarnota et al., 2010). Terrane boundaries (white dashed lines) and base metal localities are identical to those shown in Figure 1. (b) Nd_{2DM} map of Huston et al. (2014) for the central Kalgoorlie and Kurnalpi terranes – box of Figure 3a. (c) μ map of Huston et al. (2014) for the central Kalgoorlie and Kurnalpi terranes. μ represents $^{238}U/^{204}Pb$ integrated to the present, with values calculated from galena and lead telluride (altaite) Pb isotope data from VHMS and lode Au deposits of the EGS (described in Huston et al., 2005, 2014). Variations in μ can be caused by fractionation of U and Pb in the source region and/or mixing between isotopically distinct reservoirs (such as an evolved crustal source and juvenile mantle sources). Juvenile Pb isotope characteristics (low μ at Teutonic Bore correspond to a narrow, linear zone of younger granite T_{2DM} model ages. This was interpreted as a zone of extension by Huston et al. (2005, 2014), characterized by more juvenile basement.

Figure 3. Stratigraphy of the Kalgoorlie and Kurnalpi terranes, Eastern Goldfields Superterrane. (a) Stratigraphic scheme for the Eastern Goldfields Superterrane for rocks younger than ca. 2.72 Ga (after Czarnota et al., 2010). References for U-Pb zircon ages of HFSE-enriched granitic rocks are given in Hollis et al. (2015). *Main periods of VHMS mineralization:* 1, Anaconda, Nimbus; 2, Teutonic Bore, Jaguar, Bentley, King/Erayinia, Jungle Pool base metal occurrence. *Localities:* BW, Bore Well; J, Jeedamya; LB, Liberty Bore; M, Melita; MM, Murrin Murrin (i.e. Anaconda); SW, Spring Well; TB, Teutonic Bore-Jaguar-Bentley; WW, Welcome Well. (b) Detailed stratigraphic correlation for the Kambalda Sequence in the Kalgoorlie Terrane (after Hayman et al., 2015b). DCB, Devon Consols Basalt; LB, Lunnon Basalt; PB, Paringa Basalt.

Figure 4. Regional geological map of the Nimbus area based on 1:500 000 scale GSWA regional mapping (GeoVIEW at ww.dmp.wa.gov.au). The position of distal hole BODH015 is also indicated.

Figure 5. (a) Geological map of the Nimbus area (modified from Marjoribanks, 2012; and unpublished MacPhersons company reports). (b) Plan view of the mineralized lenses, diamond

drillholes and two open pits at Nimbus. Lenses of Ag mineralization are shown in silver and Zn mineralization in purple. (c) Three dimensional block model showing the multiple, steeply dipping and stacked lenses of primary sulfide mineralization at Nimbus. The depth of the Discovery Pit is approximately 90m.

Figure 6. Representative photographs of the main lithologies described herein. (a) Grading in finely bedded mudstone and sandstone from drillhole NBDH010. (b) One of several thick graded beds of interbedded mudstone and sandstone in the upper part of distal drillhole BODH015. (c) Cross-bedded quartz rich volcanic sandstones from the lower part of drillhole BODH015. (d-e) Polymict volcanic conglomerates with a variably graphitic and dacitic matrix. (f) Silicified coherent dacite cut by fine stringers of sericite. (g) Blocky, weakly mineralized monomict dacite breccia with a poorly developed and partially replaced matrix. (h) Quench fragmented monomict dacite breccia with a well-developed matrix altered to quartz-chlorite-sericite. (i) Peperitic contact between mudstone and carbonate-altered basalt. (j) Mafic hyaloclastite. (k) Well-developed varioles in basalt. (l) Polymict volcanic breccias from the top of drillhole BOD202 (associated with the Western basalt). Arrows denote clasts of varying composition. (m) Silicified and pyritic mudstone. (n) Polymict volcanic breccia from drillhole BODH015 containing clasts of mudstone, spinifex-textured komatiite and basalt (denoted by arrows). (o) Monomict volcanic breccia associated with komatiite flows (p) in distal drillhole BODH015. *Core photographs from drillholes:* NBDH010 (Fig. 6a,d-f,i-k,m), BODH015 (Fig. 6b-c,n-p), NBDH035 (Fig. 6g-h), BOD202 (Fig. 6l).

Figure 7. Downhole lithogeochemical profile of diamond drillhole NBDH010. Sudden shifts in mobile elements K_2O and CaO correspond with zones of intense sericite and carbonate alteration.

Figure 8. Representative photographs of the main styles of alteration present at Nimbus. (a) Saprock at the top of drillhole NBDH010 preserving relict volcanic textures and lithic fragments. (b) Weakly altered and silicified coherent quartz-feldspar phyric dacite. (c) Intensely silicified coherent dacite. (d) Silica-sericite-carbonate altered dacite with a foliation imparted by abundant fine sericite and

carbonate. (e) Zones of intense chloritic alteration and sericitic alteration in dacite. (f) Dacite pseudobreccia with silica-sericite-carbonate altered domains surrounded by intensely sericite altered domains. Note the progressive alteration of the 'clasts'. (g) Foliated fuchsitic pseudobreccia with chloritic patches surrounding domains of intensely silica-sericite altered dacite. (h) Pseudobrecciated dacite near the contact with the Northeast basalt in NBDH010. Apparent clasts of silica-sericite altered dacite are surrounded by a network of chlorite, fuchsite and sericite. (i) Hydrothermal silica filling fractures in a silica-sericite altered dacite. (j) Intensely silicified dacite partially replaced by pyrite and cut by sericite veinlets. (k) Altered monomict dacite breccia with quartz-carbon altered dacite clasts in an altered matrix dominated by fine chlorite-carbonate-quartz. Some spots of pyrite are present and possible patches of carbonaceous mudstone. (l) Dolomite altered metabasalt. Core photographs from drillholes: NBDH010 (Fig. 8a,c-d,h), BOD202 (Fig. 8b,e-g,i-j,l), NBDH035 (Fig. 8k). Mineralogy: Chlor, chlorite; Dol, dolerite; Fsp, feldspar (altered); Grap, graphite; Plagio, plagioclase; Pyr, pyrite; Qtz, quartz; Ser, sericite.

Figure 9. Representative photographs of the main styles of alteration present at Nimbus. (a) Saprock at the top of drillhole NBDH010 preserving relict volcanic textures and lithic fragments. (b) Weakly altered and silicified coherent quartz-feldspar phyric dacite. (c) Intensely silicified coherent dacite. (d) Silica-sericite-carbonate altered dacite with a foliation imparted by abundant fine sericite and carbonate. (e) Zones of intense chloritic alteration and sericitic alteration in dacite. (f) Dacite pseudobreccia with silica-sericite-carbonate altered domains surrounded by intensely sericite altered domains. Note the progressive alteration of the 'clasts'. (g) Foliated fuchsitic pseudobreccia with chloritic patches surrounding domains of intensely silica-sericite altered dacite. (h) Pseudobrecciated dacite near the contact with the Northeast basalt in NBDH010. Apparent clasts of silica-sericite altered dacite are surrounded by a network of chlorite, fuchsite and sericite. (i) Hydrothermal silica filling fractures in a silica-sericite altered dacite. (j) Intensely silicified dacite partially replaced by pyrite and cut by sericite veinlets. (k) Altered monomict dacite breccia with quartz-carbon altered dacite clasts in an altered matrix dominated by fine chlorite-carbonate-quartz. Some spots of pyrite are present and possible patches of carbonaceous mudstone. (l) Dolomite altered metabasalt. *Core photographs from*

drillholes: NBDH010 (Fig. 9a,c-d,h), BOD202 (Fig. 9b,e-g,i-j,l), NBDH035 (Fig. 9k). *Mineralogy:* Chlor, chlorite; Dol, dolerite; Fsp, feldspar (altered); Grap, graphite; Plagio, plagioclase; Pyr, pyrite; Qtz, quartz; Ser, sericite.

Figure 10. Immobile element geochemistry for felsic and mafic rocks from Nimbus. (a) Zr/TiO_2 vs Nb/Y immobile-element discrimination diagram for volcanic rocks (after Pearce, 1996). Note the bimodal nature of the stratigraphy hosting the Nimbus deposit. (b-d) Comparison of mafic rocks to data from elsewhere in the Eastern Goldfields Superterrane: Nb vs TiO_2, La vs TiO_2 and Th vs TiO_2. All mafic rocks are similar to the ~2.7 Ga Lunnon Basalt and the low-Th suite of Barnes et al. (2012). (e-f) VHMS fertility diagrams of Lesher et al. (1986; Fig. 10e) and Hart et al. (2004; Fig. 10f). All samples of dacite from Nimbus are calc-alkaline and of FI affinity characterised by low HFSE concentrations and high Zr/Y and La/Yb ratios. By contrast, samples from Teutonic Bore and Jaguar plot in the FII and FIII fields indicative of VHMS prospective Archaean felsic rocks and shallow crustal melting. (g-h) Chondrite normalized REE spider diagrams for mafic/ultramafic and felsic samples from Nimbus. (i) Chondrite normalized REE spider diagram for andesites and felsic rocks from Teutonic Bore and Jaguar. *Data sources:* Barnes et al. (2012), Barnes and Van Kranendonk (2014), Belford (2010), Hollis et al. (2015), Hollis (unpublished).

Figure 11. Tectonic discrimination diagrams for samples from Nimbus, Teutonic Bore (Hollis, unpublished) and the Lunnon, Devon Consols and Paringa basalts of the Kambalda Sequence (Barnes et al., 2012). (a) La-Y-Nb diagram of Cabanis and Lecolle (1989) (b) Zr-Y-Ti diagram of Pearce and Cann (1973). (c) Th/Yb vs Nb/Yb diagram of Pearce (2008; 2014). (d)TiO_2/Yb vs Nb/Yb diagram of Pearce (2014).

Figure 12. SHRIMP U-Pb zircon concordia diagrams and weighted mean ages for two samples dated from the Nimbus deposit (see Supplementary Table 2 for data). Representative zircon grains are shown along with those discussed in the text and selected $\delta^{18}O$ data. Sample NIM011 is from the coherent

dacite facies under the Discovery Pit (NBDH035, ~291m), whereas SPHGEO1 is from under the East Pit (NBDH010, ~285m) (see Fig. 5 for locations).

Figure 13. Zircon $\delta^{18}O$ data from NIM011 and SPHGEO1 (Nimbus dacite). (a) $\delta^{18}O$ zircon data from Nimbus dacites (Supplementary Table 5) are shown relative to other zircon $\delta^{18}O$ data from six key settings; Archean cratons, continental flood basalts, intraplate volcanics, rift volcanics, volcanic arcs and mid-ocean ridge basalt (MORB). Data for zircons are from the GEOROC database (Sarbas and Nohl, 2008; references listed below), Cavosie et al. (2009), Valley et al. (2005) and the database of Spencer et al. (2014a; references listed below). All compiled data are provided in Supplementary Table 6. The $\delta^{18}O$ compilation for whole-rock systems is taken from Bindeman (2008), Valley et al. (2005), Muehlenbachs (1998), Eiler (2001), Hoefs (2008), Sharp (2007), Arthur et al. (1983), Gregory and Taylor (1981), Land and Lynch (1996), Shields and Veizer (2002), Knauth and Lowe (2003) and Perry Jr and Lefticariu (2003). Thinner data-bars represent single values with an inferred 10‰ range. Thicker data-bars represent a range of real values. Data for mantle-zircon range (2σ) taken from Valley et al. (2005) and shown as the red vertical field. (b) $\delta^{18}O$ vs. $^{207}Pb/^{206}Pb$ age for NIM011 and SPHGEO1 shown using individual spot $^{207}Pb/^{206}Pb$ ages; and (c) $\delta^{18}O$ for SPHGEO1; and (d) $\delta^{18}O$ for NIM011. All error bars are 2σ. *Data sources from GEOROC:* Bindeman et al. (2008), Bindeman and Valley (2000, 2001, 2002, 2003), Chen et al. (2014), Gilliam and Valley (1997), Kemp et al. (2006), King et al. (2000), Kitajima et al. (2012), Li et al. (2010), Liu and Zhang et al. (2013), Monani and Valley (2001), Siebel et al. (2011), Spencer et al. (2014b), Su et al. (2011), Tichomirowa et al. (2013), Upton et al. (1999), Zheng et al. (2008). *Data sources listed by Spencer et al. (2014a):* Arthur et al. (1983), Bolhar et al. (2008), Dai et al. (2011), Gregory and Taylor (1981), Heilimo et al. (2013), Jiang et al. (2012), King and Valley (2001), King et al. (1998), Lackey et al. (2005, 2006), Land and Lynch (1996), Li et al. (2012), Peck et al. (2001), Perry Jr and Lefticariu (2003), Roberts et al. (2013), Shields and Veizer (2002), Wang et al. (2013), Zheng et al. (2012).

Figure 14. Pb isotope ratios for samples of galena analysed from Nimbus (see Supplementary Table 7 for data). Also included is data from epigenetic Au deposits of the Norseman Wiluna Belt and VHMS deposits of the Teutonic Bore camp. *Data sources:* Vaaskoki (1985), Browning et al. (1987), Dahl et al. (1987), McNaughton et al. (1990), McNaughton and Groves (1996), Huston et al. (2014).

Figure 15. Schematic model for the evolution of the Nimbus Ag-Zn-(Au) deposit. (a) Cross section assuming present-day younging to the NE. The stratigraphy consists of stacked dacitic rocks (yellow) with hyaloclastite-rich margins, intruded by broadly coeval, high-level mafic sills (green). Both mafic and felsic lithologies have peperitic relationships with less-frequent graphitic mudstones (dark grey). (b) Hydrothermal fluids were focussed through hyaloclastite in both mafic and felsic lithologies (orange), along lithological boundaries (pink), and through fractures in the coherent dacite facies. (c) Massive sulfide mineralization (red) occurs primarily in dacite hyaloclastite associated with intense quartz-sericite±chlorite alteration (orange). Zones of stringer sulfides occur in the coherent dacite facies characterized by weaker quartz-sericite-carbonate alteration (grey). Mafic rocks are dominated by quartz-carbonate-chlorite and disseminated sulfides. Mafic-felsic contacts are characterized by abundant quartz-sericite-carbonate-fuchsite±chlorite (pale green). Weakly altered dacitic rocks (yellow) are characterised by silicification and/or albitic alteration. The interpreted position of the Discovery and East pits are shown, along with drillhole NBHD010 (discounting the effects of regional deformation).

Supplementary Table 1. Whole rock geochemical data for samples analysed from the Nimbus stratigraphy and regional drillhole BODH015.

Supplementary Table 2. SHRIMP U-Pb zircon data for samples of dacite from the Nimbus stratigraphy.

Supplementary Table 3. SHRIMP U-Pb zircon data for primary and secondary standards.

Supplementary Table 4. $\delta^{18}O$ data for primary (TEMORA) and secondary (M257 and OGC) standards collected during the analytical session.

Supplementary Table 5. $\delta^{18}O$ data for dated zircons from NIM011 and SPHGEO1.

Supplementary Table 6. Compiled global database for O isotopes.

Supplementary Table 7. Pb isotopic data normalised to common lead standard NIST 981. The result is the average of three datasets.

Sample ID	Lithology	$^{206}Pb/^{204}Pb$	$^{207}Pb/^{204}Pb$	$^{208}Pb/^{204}Pb$	$\mu={}^{238}U/^{204}Pb$ Abitibi-Wawa
NBDH013_334m	Dacite with disseminated and stringer sphalerite-pyrite. Narrow, coarsely crystalline bands of galena and chalcopyrite are also present.	13.49	14.68	33.28	8.34
NBDH035_175m	Dacite with stringers of high- and low-Fe sphalerite, pyrite, chalcopyrite and galena.	13.49	14.68	33.27	8.35

Supplementary Figure 1. Representative photomicrographs of hydrothermal alteration at Nimbus (all images except Fig. 1i are under crossed polarised light). (a) Sample 183348: Weakly quartz-sericite-carbonated altered quartz-feldspar porphyritic dacite. Randomly oriented feldspar phenocrysts are well preserved, though slightly dusted with sericite. (b) Sample 183354: Sheared moderately sericite-quartz-(carbonate) altered quartz-feldspar porphyritic dacite. (c) Sample 183355: Quartz-carbonate-(sericite) altered quartz-feldspar porphyritic dacite. The groundmass is extensively replaced by quartz and carbonate with lesser sericite and patches of epidote and chlorite. (d) Sample 182575: Sheared moderately sericite-quartz-(carbonate) altered quartz-feldspar porphyritic dacite similar to Figure 10b, with extensive pyrite mineralization and coarse patches of carbonate. (e) Sample 183353: Quartz-carbonate-(sericite) altered quartz-feldspar porphyritic dacite. Pyrite stringers are brecciated parallel to the deformation fabric and sericite veinlets. (f) Sample 182587: Mafic hyaloclastite with well-preserved primary igneous textures in clasts. The groundmass is extensively altered to dolomite-chlorite-quartz. Fine pyrite and sphalerite are disseminated throughout the matrix. (g) Sample 182567: Intensely dolomite-altered mafic rock sampled from the Western Basalt. The groundmass comprises a fine mixture of dolomite-chlorite-quartz and separates coarse patches of dolomite. (h) Sample 183343: Moderately dolomite-chlorite-quartz altered coherent mafic rock from the Northeast Basalt. Minor patches of pyrite and epidote occur throughout the groundmass. Relic plagioclase laths are still apparent. (i) Sample 182583: Silicified and quartz-brecciated, pyritic mudstone. Thin bands of recrystallized quartz with pyrite alternated with graphitic mudstone. All samples are from drillhole NBDH010, except Figures 2d,g (which are from drillhole BOD202).

Supplementary Figure 2. U-Pb zircon concordia for standard OGC.

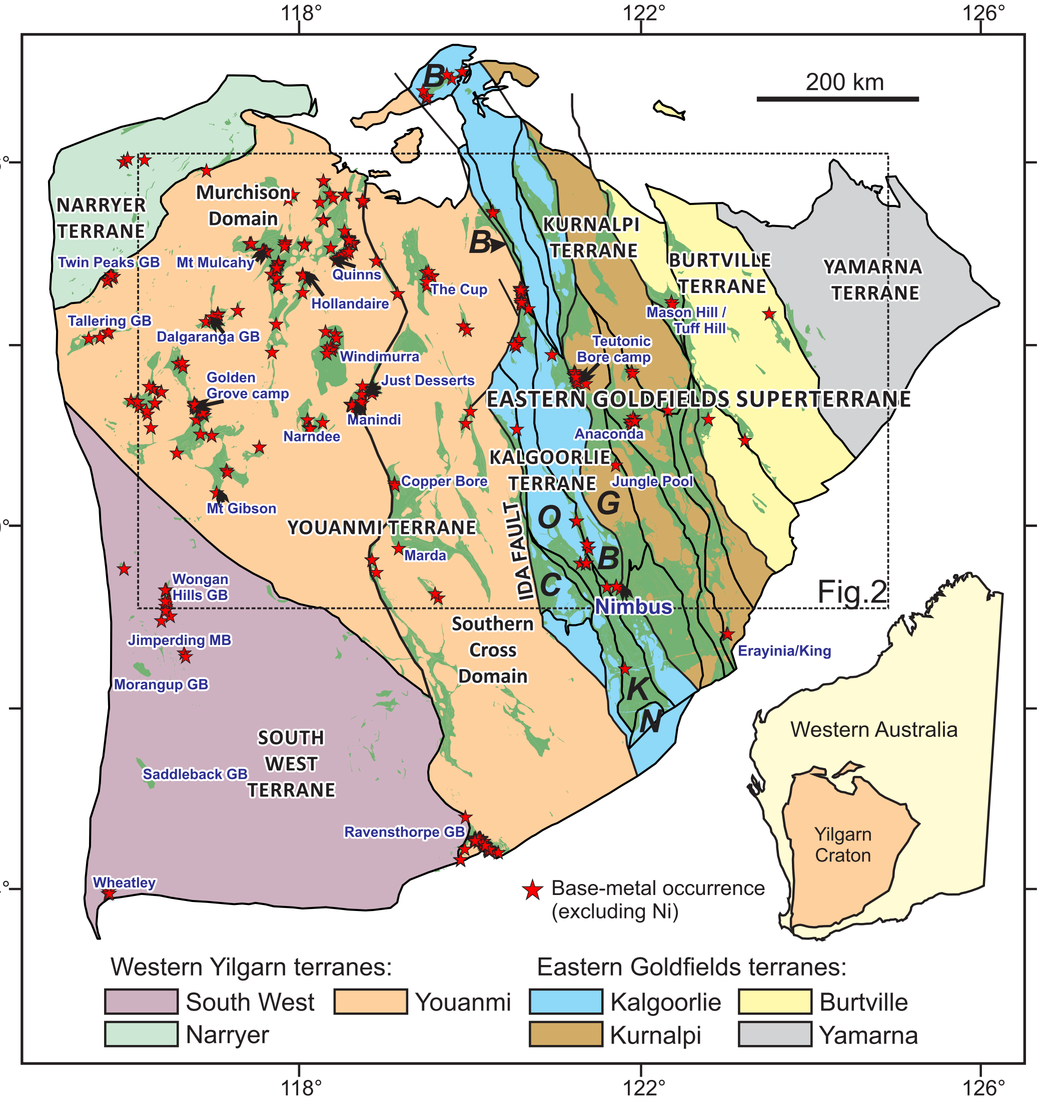

118°
122°
126°
-26°
-30°
-34°
200 km
NARRYER TERRANE
Murchison Domain
KURNALPI TERRANE
BURTVILLE TERRANE
YAMARNA TERRANE
Twin Peaks GB
Mt Mulcahy
Quinns
Hollandaire
The Cup
Mason Hill / Tuff Hill
Tallering GB
Dalgaranga GB
Windimurra
Teutonic Bore camp
Golden Grove camp
Just Desserts
EASTERN GOLDFIELDS SUPERTERRANE
Manindi
Narndee
Anaconda
KALGOORLIE TERRANE
Copper Bore
Jungle Pool
Mt Gibson
YOUANMI TERRANE
IDA FAULT
Marda
Wongan Hills GB
Nimbus
Fig.2
Southern Cross Domain
Jimperding MB
Erayinia/King
Morangup GB
Western Australia
SOUTH WEST TERRANE
Saddleback GB
Yilgarn Craton
Ravensthorpe GB
Wheatley
Base-metal occurrence (excluding Ni)
Western Yilgarn terranes:
South West
Youanmi
Narryer
Eastern Goldfields terranes:
Kalgoorlie
Burtville
Kurnalpi
Yamarna

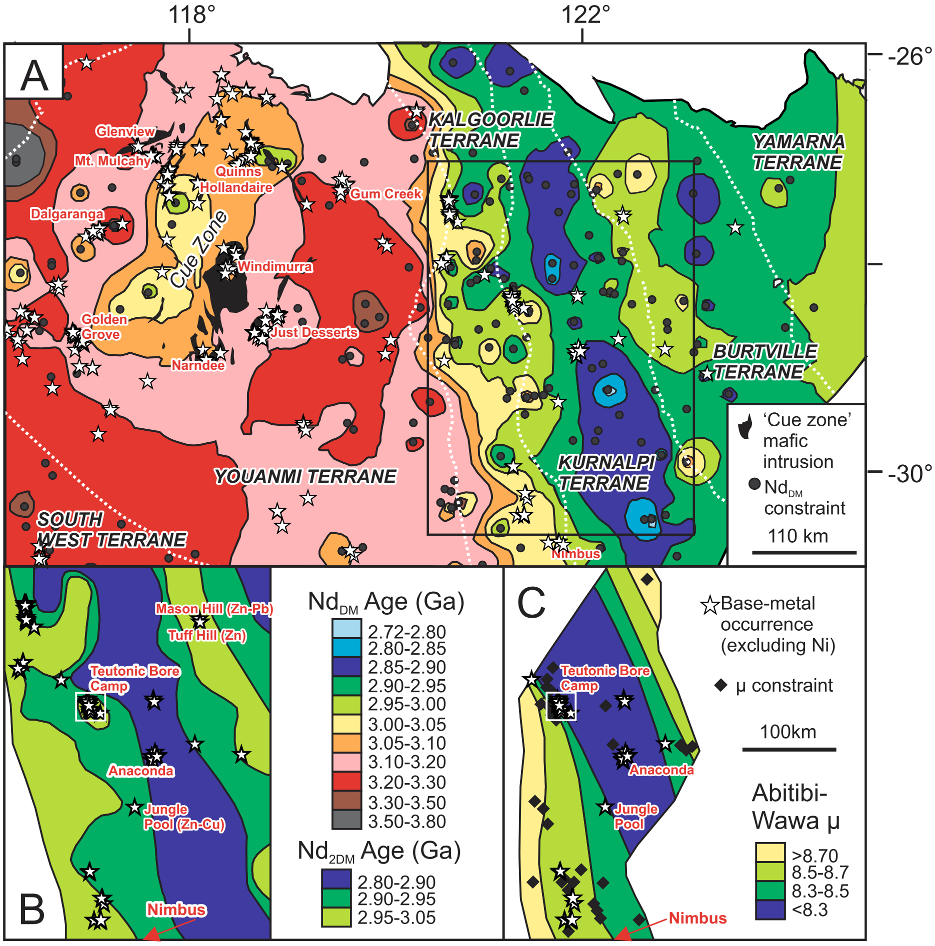
118°
122°
-26°
-30°
A
KALGOORLIE TERRANE
YAMARNA TERRANE
BURTVILLE TERRANE
KURNALPI TERRANE
YOUANMI TERRANE
SOUTH WEST TERRANE
Glenview
Mt. Mulcahy
Quinns
Hollandaire
Gum Creek
Dalgaranga
Cue Zone
Windimurra
Golden Grove
Just Desserts
Narndee
Nimbus
'Cue zone' mafic intrusion
Nd_{DM} constraint
110 km
B
Mason Hill (Zn-Pb)
Tuff Hill (Zn)
Teutonic Bore Camp
Anaconda
Jungle Pool (Zn-Cu)
Nimbus
Nd_{DM} Age (Ga)
2.72-2.80
2.80-2.85
2.85-2.90
2.90-2.95
2.95-3.00
3.00-3.05
3.05-3.10
3.10-3.20
3.20-3.30
3.30-3.50
3.50-3.80
Nd_{2DM} Age (Ga)
2.80-2.90
2.90-2.95
2.95-3.05
C
Teutonic Bore Camp
Anaconda
Jungle Pool
Nimbus
Base-metal occurrence (excluding Ni)
μ constraint
100km
Abitibi-Wawa μ
>8.70
8.5-8.7
8.3-8.5
<8.3

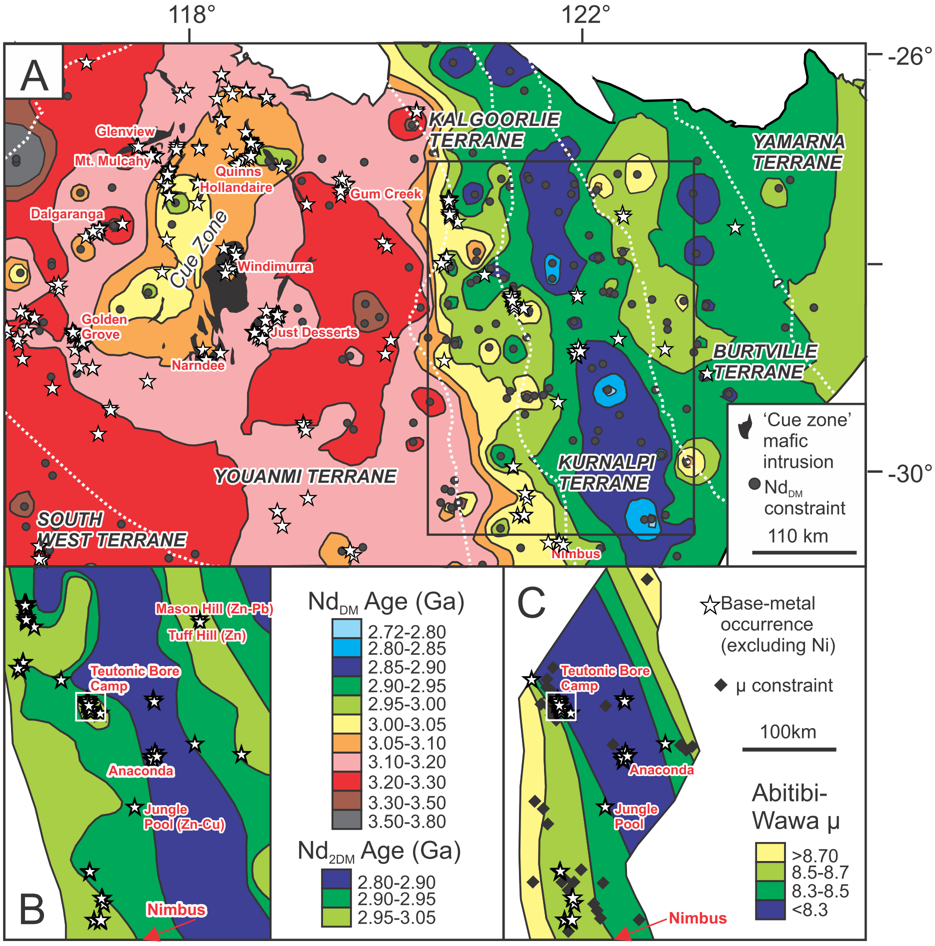

118°
122°
-26°
-30°
A
KALGOORLIE TERRANE
YAMARNA TERRANE
BURTVILLE TERRANE
KURNALPI TERRANE
YOUANMI TERRANE
SOUTH WEST TERRANE
Cue Zone
Glenview
Mt. Mulcahy
Quinns
Hollandaire
Gum Creek
Dalgaranga
Windimurra
Golden Grove
Just Desserts
Narndee
Nimbus
'Cue zone' mafic intrusion
Nd_{DM} constraint
110 km
B
Mason Hill (Zn-Pb)
Tuff Hill (Zn)
Teutonic Bore Camp
Anaconda
Jungle Pool (Zn-Cu)
Nimbus
Nd_{DM} Age (Ga)
2.72-2.80
2.80-2.85
2.85-2.90
2.90-2.95
2.95-3.00
3.00-3.05
3.05-3.10
3.10-3.20
3.20-3.30
3.30-3.50
3.50-3.80
Nd_{2DM} Age (Ga)
2.80-2.90
2.90-2.95
2.95-3.05
C
Teutonic Bore Camp
Anaconda
Jungle Pool
Nimbus
Base-metal occurrence (excluding Ni)
μ constraint
100km
Abitibi-Wawa μ
>8.70
8.5-8.7
8.3-8.5
<8.3

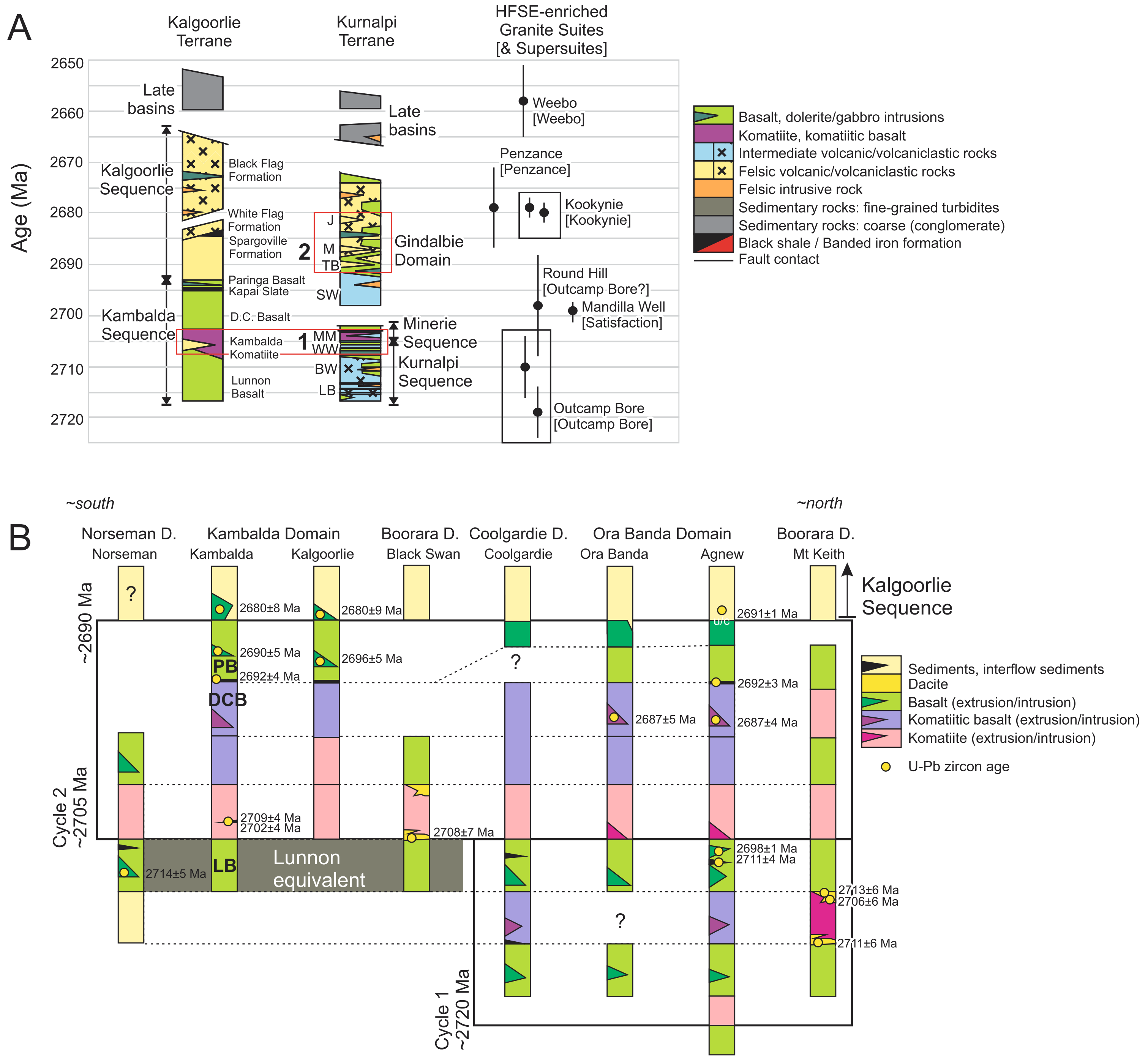
A
Kalgoorlie Terrane
Kurnalpi Terrane
HFSE-enriched Granite Suites [& Supersuites]
Age (Ma)
Late basins
Kalgoorlie Sequence
Black Flag Formation
White Flag Formation
Spargoville Formation
Paringa Basalt
Kapai Slate
D.C. Basalt
Kambalda Sequence
Kambalda Komatiite
Lunnon Basalt
Gindalbie Domain
Minerie Sequence
Kurnalpi Sequence
Weebo [Weebo]
Penzance [Penzance]
Kookynie [Kookynie]
Round Hill [Outcamp Bore?]
Mandilla Well [Satisfaction]
Outcamp Bore [Outcamp Bore]
Basalt, dolerite/gabbro intrusions
Komatiite, komatiitic basalt
Intermediate volcanic/volcaniclastic rocks
Felsic volcanic/volcaniclastic rocks
Felsic intrusive rock
Sedimentary rocks: fine-grained turbidites
Sedimentary rocks: coarse (conglomerate)
Black shale / Banded iron formation
Fault contact
B
~south
~north
Norseman D. Norseman
Kambalda Domain Kambalda Kalgoorlie
Boorara D. Black Swan
Coolgardie D. Coolgardie
Ora Banda Domain Ora Banda Agnew
Boorara D. Mt Keith
Kalgoorlie Sequence
~2690 Ma
Cycle 2 ~2705 Ma
Cycle 1 ~2720 Ma
2680±8 Ma
2680±9 Ma
2691±1 Ma
2690±5 Ma
2696±5 Ma
2692±4 Ma
2692±3 Ma
2687±5 Ma
2687±4 Ma
2709±4 Ma
2702±4 Ma
2708±7 Ma
2714±5 Ma
2698±1 Ma
2711±4 Ma
2713±6 Ma
2706±6 Ma
2711±6 Ma
PB
DCB
LB
Lunnon equivalent
Sediments, interflow sediments
Dacite
Basalt (extrusion/intrusion)
Komatiitic basalt (extrusion/intrusion)
Komatiite (extrusion/intrusion)
U-Pb zircon age

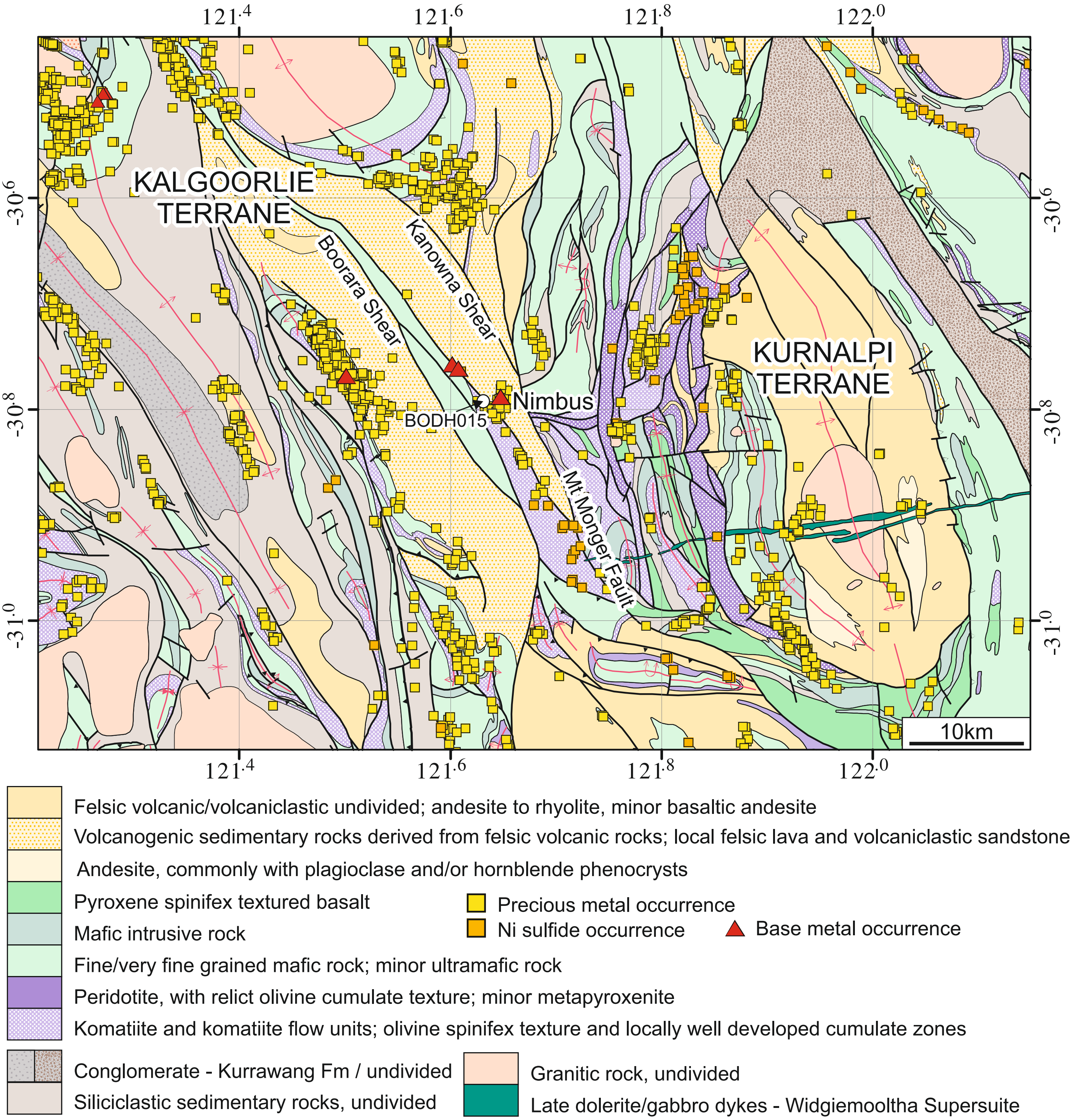
121.4
121.6
121.8
122.0
-30.6
-30.8
-31.0
KALGOORLIE TERRANE
KURNALPI TERRANE
Boorara Shear
Kanowna Shear
Mt Monger Fault
Nimbus
BODH015
10km
Felsic volcanic/volcaniclastic undivided; andesite to rhyolite, minor basaltic andesite
Volcanogenic sedimentary rocks derived from felsic volcanic rocks; local felsic lava and volcaniclastic sandstone
Andesite, commonly with plagioclase and/or hornblende phenocrysts
Pyroxene spinifex textured basalt
Mafic intrusive rock
Fine/very fine grained mafic rock; minor ultramafic rock
Peridotite, with relict olivine cumulate texture; minor metapyroxenite
Komatiite and komatiite flow units; olivine spinifex texture and locally well developed cumulate zones
Precious metal occurrence
Ni sulfide occurrence
Base metal occurrence
Conglomerate - Kurrawang Fm / undivided
Siliciclastic sedimentary rocks, undivided
Granitic rock, undivided
Late dolerite/gabbro dykes - Widgiemooltha Supersuite

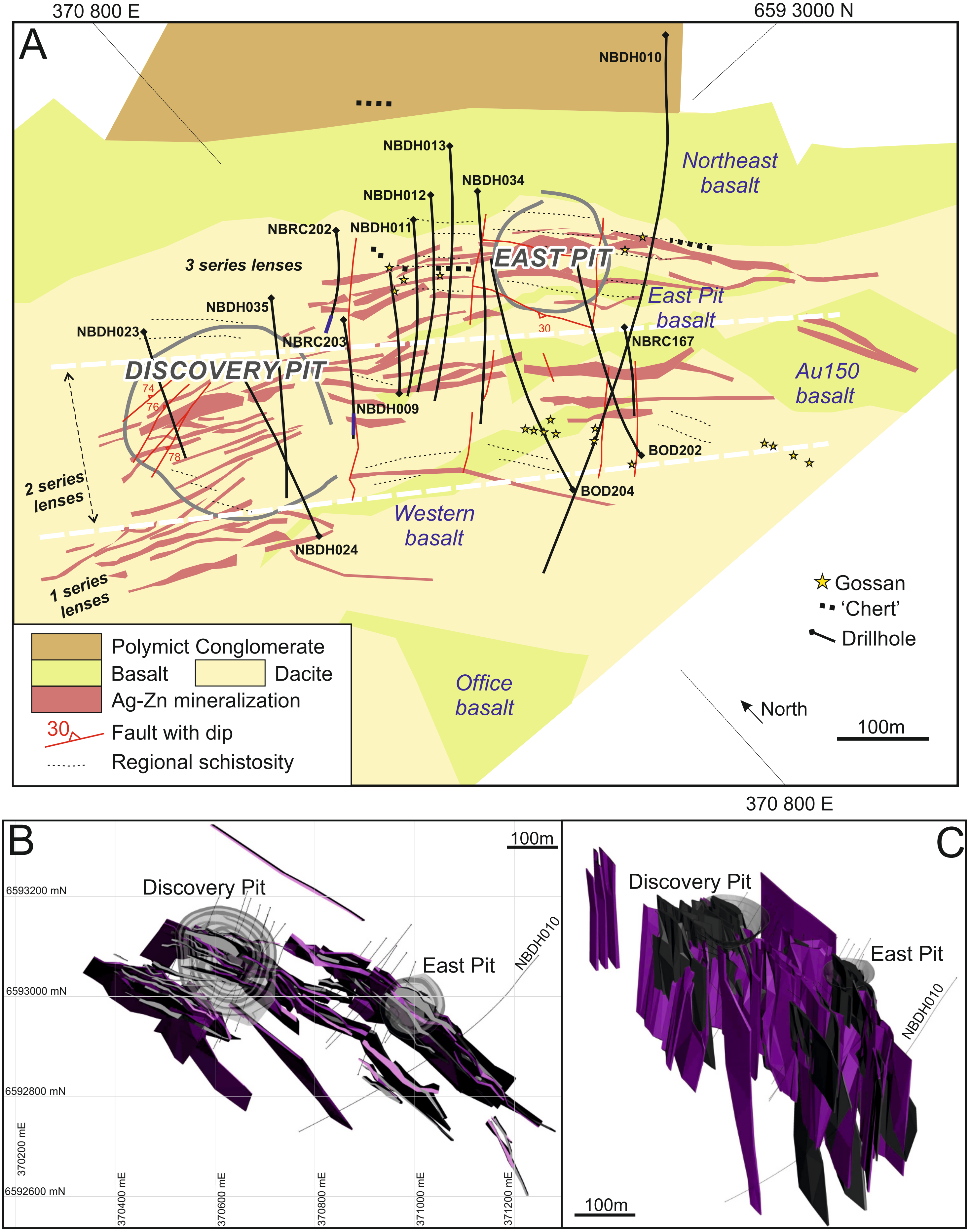

370 800 E
659 3000 N
A
NBDH010
NBDH013
NBDH034
NBDH012
NBRC202
NBDH011
Northeast basalt
3 series lenses
EAST PIT
East Pit basalt
NBDH035
NBDH023
NBRC203
30
NBRC167
DISCOVERY PIT
Au150 basalt
74
76
78
NBDH009
BOD202
2 series lenses
BOD204
Western basalt
NBDH024
1 series lenses
Gossan
'Chert'
Drillhole
Polymict Conglomerate
Basalt
Dacite
Ag-Zn mineralization
30
Fault with dip
Regional schistosity
Office basalt
North
100m
370 800 E
B
100m
6593200 mN
Discovery Pit
East Pit
NBDH010
6593000 mN
6592800 mN
370200 mE
6592600 mN
370400 mE
370600 mE
370800 mE
371000 mE
371200 mE
C
Discovery Pit
East Pit
NBDH010
100m

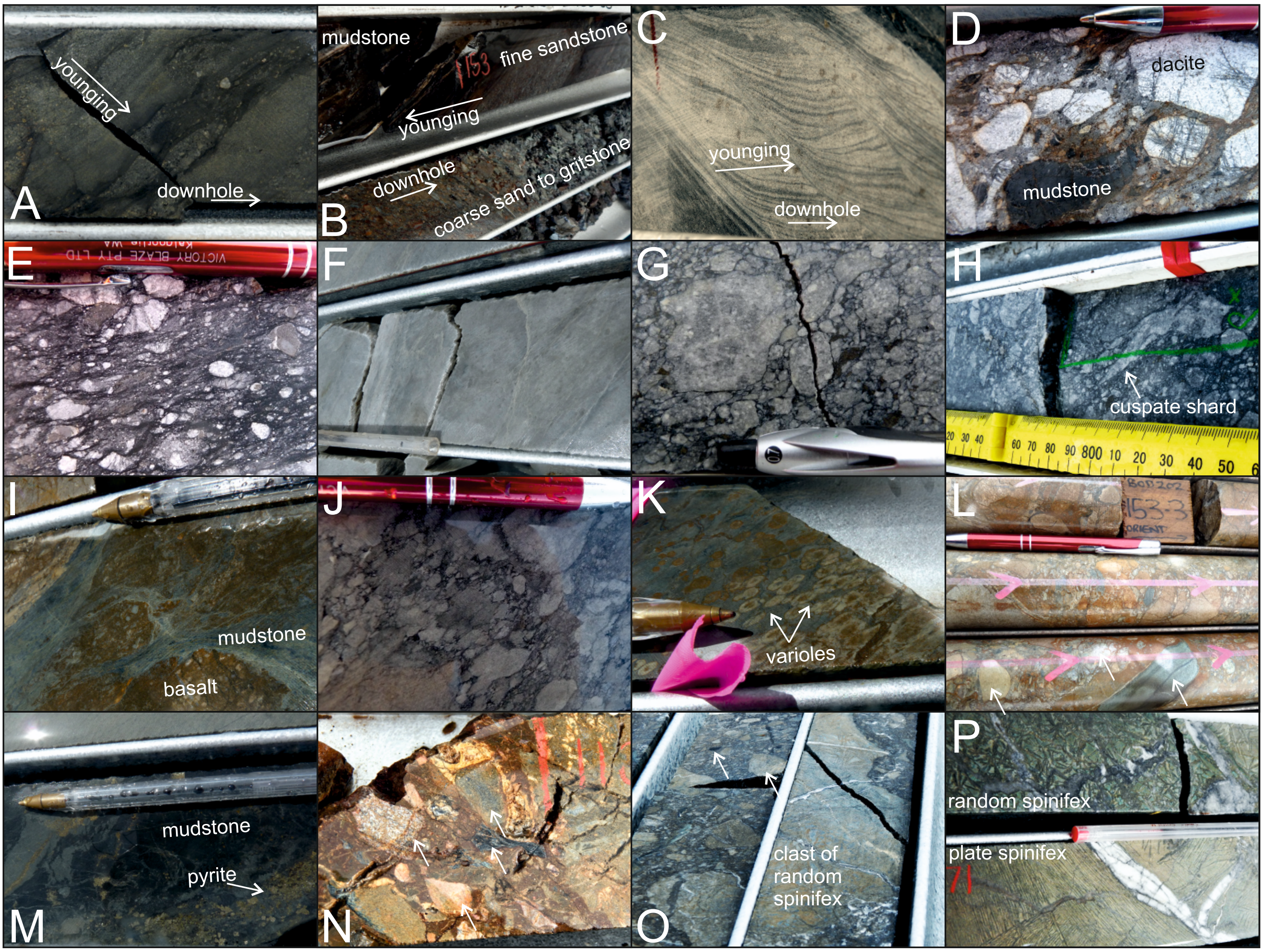
A
younging
downhole
B
mudstone
fine sandstone
younging
downhole
coarse sand to gritstone
C
younging
downhole
D
dacite
mudstone
E
F
G
H
cuspate shard
I
mudstone
basalt
J
K
varioles
L
M
mudstone
pyrite
N
O
clast of
random
spinifex
P
random spinifex
plate spinifex

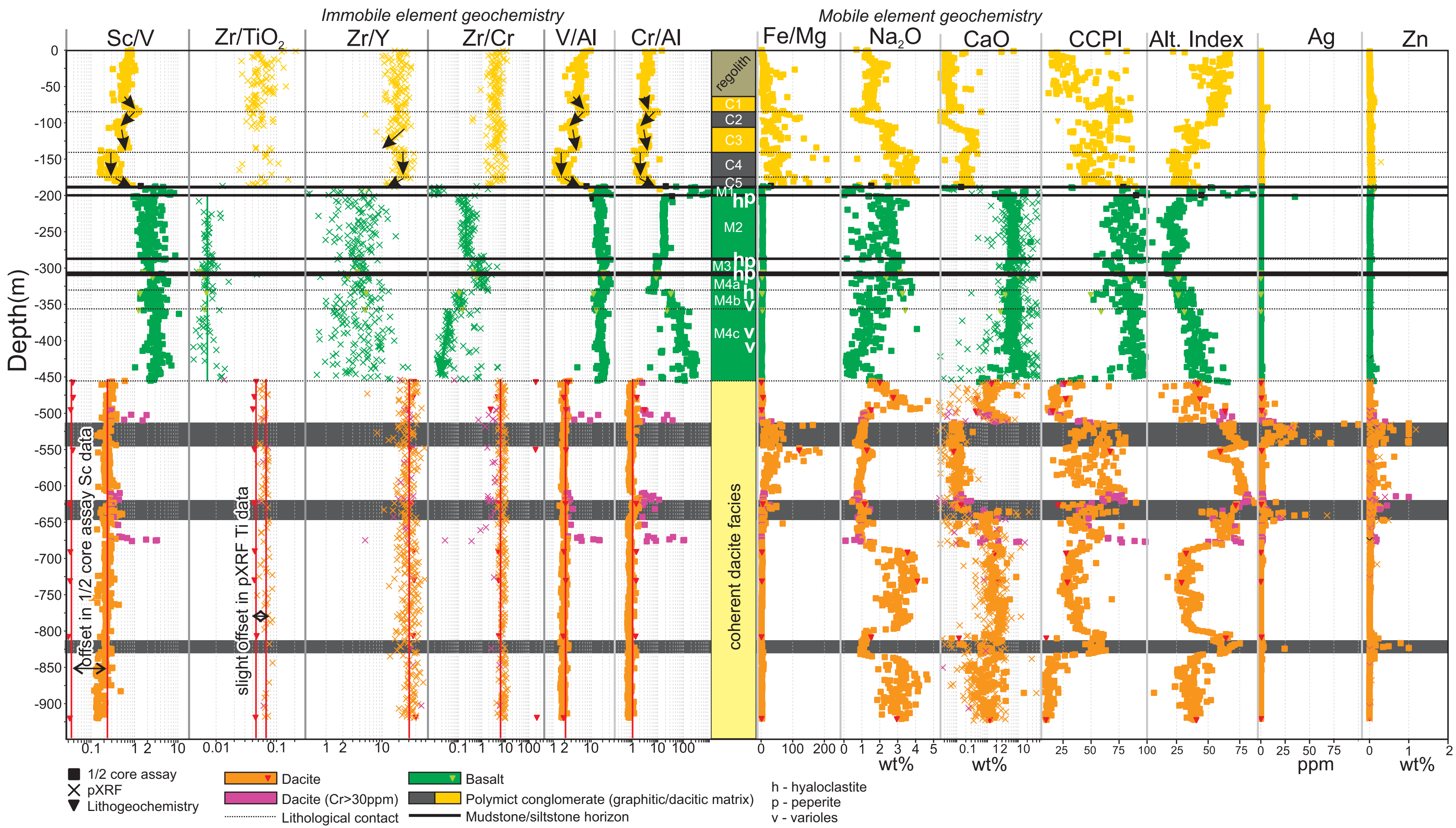

Immobile element geochemistry
Mobile element geochemistry
Sc/V
Zr/TiO2
Zr/Y
Zr/Cr
V/Al
Cr/Al
Fe/Mg
Na2O
CaO
CCPI
Alt. Index
Ag
Zn
Depth(m)
regolith
C1
C2
C3
C4
C5
M1
M2
M3
M4a
M4b
M4c
hp
h
v
coherent dacite facies
offset in 1/2 core assay Sc data
slight offset in pXRF Ti data
wt%
ppm
1/2 core assay
pXRF
Lithogeochemistry
Dacite
Dacite (Cr>30ppm)
Lithological contact
Basalt
Polymict conglomerate (graphitic/dacitic matrix)
Mudstone/siltstone horizon
h - hyaloclastite
p - peperite
v - varioles

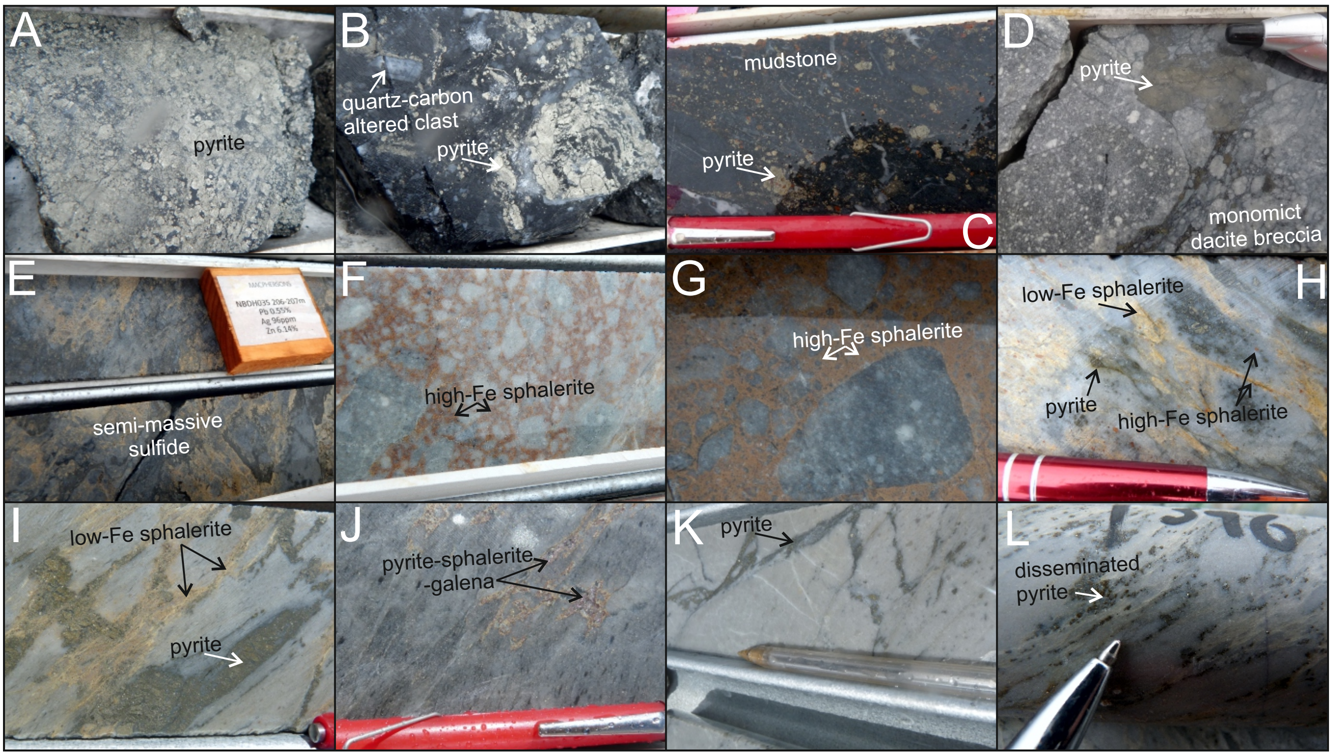

A
pyrite
B
quartz-carbon altered clast
pyrite
C
mudstone
pyrite
D
pyrite
monomict dacite breccia
E
MACPHERSONS
NBDH035 206-207m
Pb 0.55%
Ag 96ppm
Zn 6.14%
semi-massive sulfide
F
high-Fe sphalerite
G
high-Fe sphalerite
H
low-Fe sphalerite
pyrite
high-Fe sphalerite
I
low-Fe sphalerite
pyrite
J
pyrite-sphalerite -galena
K
pyrite
L
disseminated pyrite

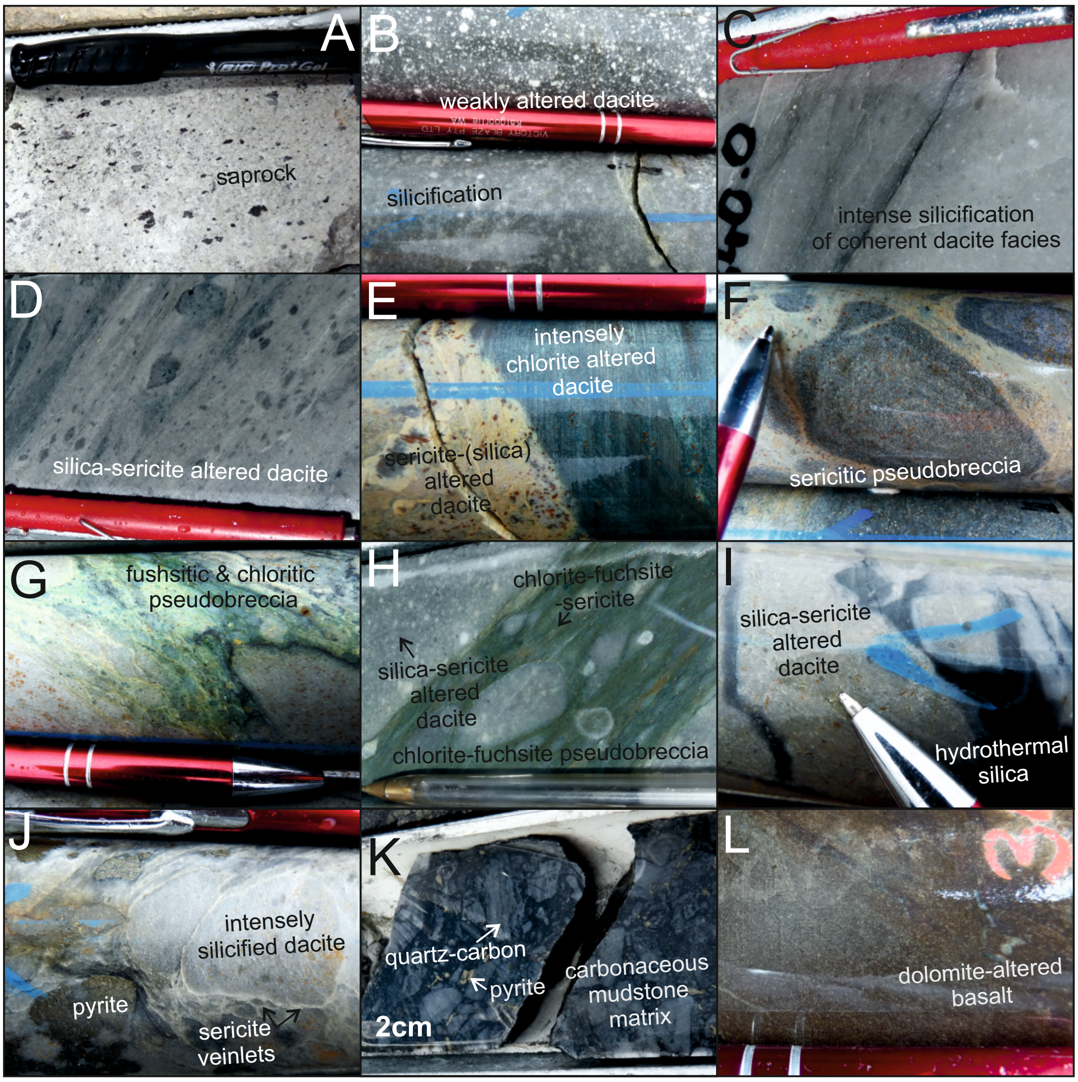
A
saprock
B
weakly altered dacite
silicification
C
intense silicification
of coherent dacite facies
D
silica-sericite altered dacite
E
intensely
chlorite altered
dacite
sericite-(silica)
altered
dacite
F
sericitic pseudobreccia
G
fushsitic & chloritic
pseudobreccia
H
chlorite-fuchsite
-sericite
silica-sericite
altered
dacite
chlorite-fuchsite pseudobreccia
I
silica-sericite
altered
dacite
hydrothermal
silica
J
intensely
silicified dacite
pyrite
sericite
veinlets
K
quartz-carbon
pyrite
carbonaceous
mudstone
matrix
2cm
L
dolomite-altered
basalt

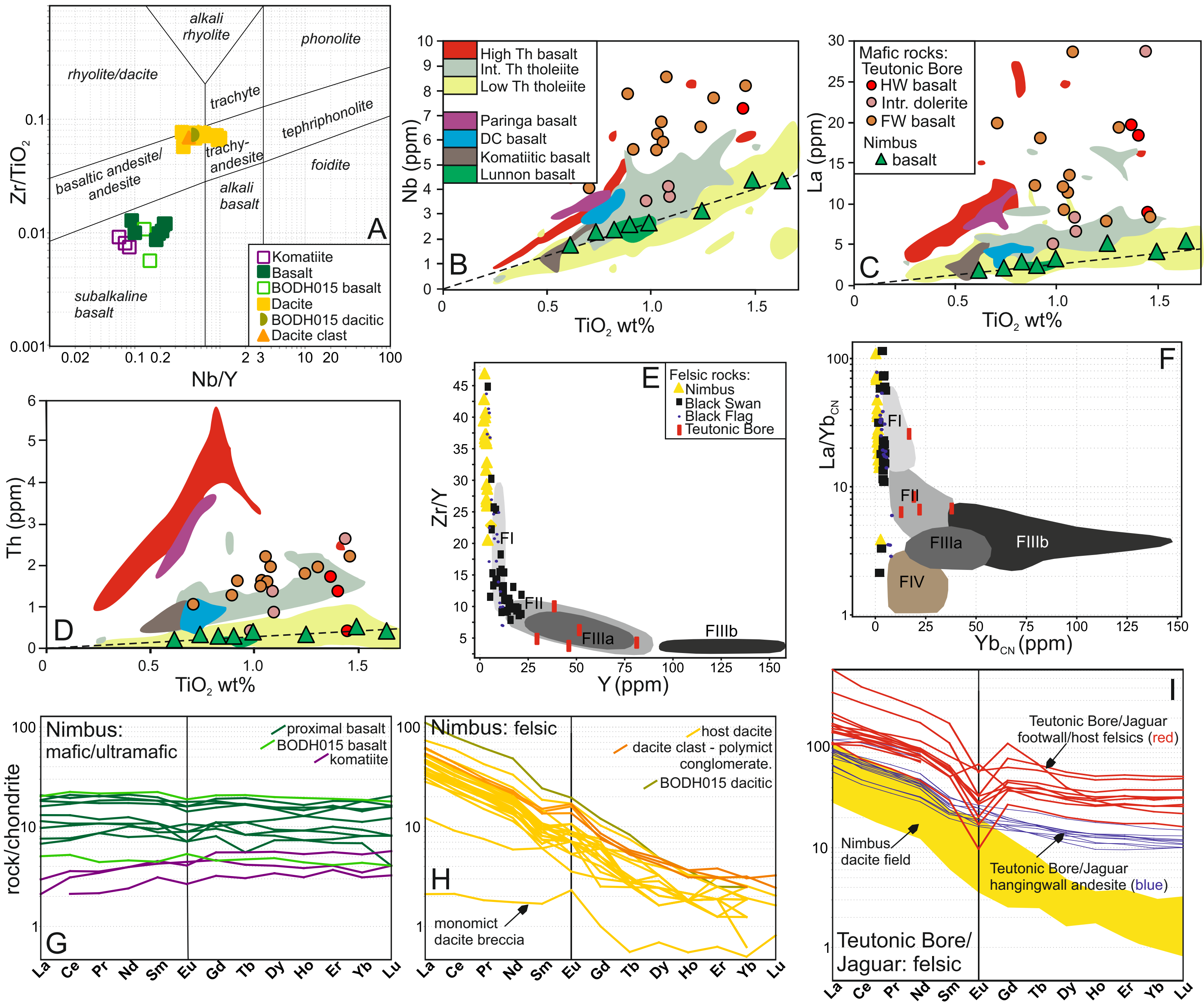

A
alkali rhyolite
phonolite
rhyolite/dacite
trachyte
tephriphonolite
basaltic andesite/ andesite
trachy-andesite
foidite
alkali basalt
subalkaline basalt
Komatiite
Basalt
BODH015 basalt
Dacite
BODH015 dacitic
Dacite clast
Zr/TiO2
Nb/Y
B
High Th basalt
Int. Th tholeiite
Low Th tholeiite
Paringa basalt
DC basalt
Komatiitic basalt
Lunnon basalt
Nb (ppm)
TiO2 wt%
C
Mafic rocks:
Teutonic Bore
HW basalt
Intr. dolerite
FW basalt
Nimbus
basalt
La (ppm)
TiO2 wt%
D
Th (ppm)
TiO2 wt%
E
Felsic rocks:
Nimbus
Black Swan
Black Flag
Teutonic Bore
FI
FII
FIIIa
FIIIb
Zr/Y
Y (ppm)
F
FI
FII
FIIIa
FIIIb
FIV
La/YbCN
YbCN (ppm)
G
Nimbus: mafic/ultramafic
proximal basalt
BODH015 basalt
komatiite
rock/chondrite
H
Nimbus: felsic
host dacite
dacite clast - polymict conglomerate.
BODH015 dacitic
monomict dacite breccia
I
Teutonic Bore/Jaguar footwall/host felsics (red)
Nimbus dacite field
Teutonic Bore/Jaguar hangingwall andesite (blue)
Teutonic Bore/ Jaguar: felsic
La Ce Pr Nd Sm Eu Gd Tb Dy Ho Er Yb Lu

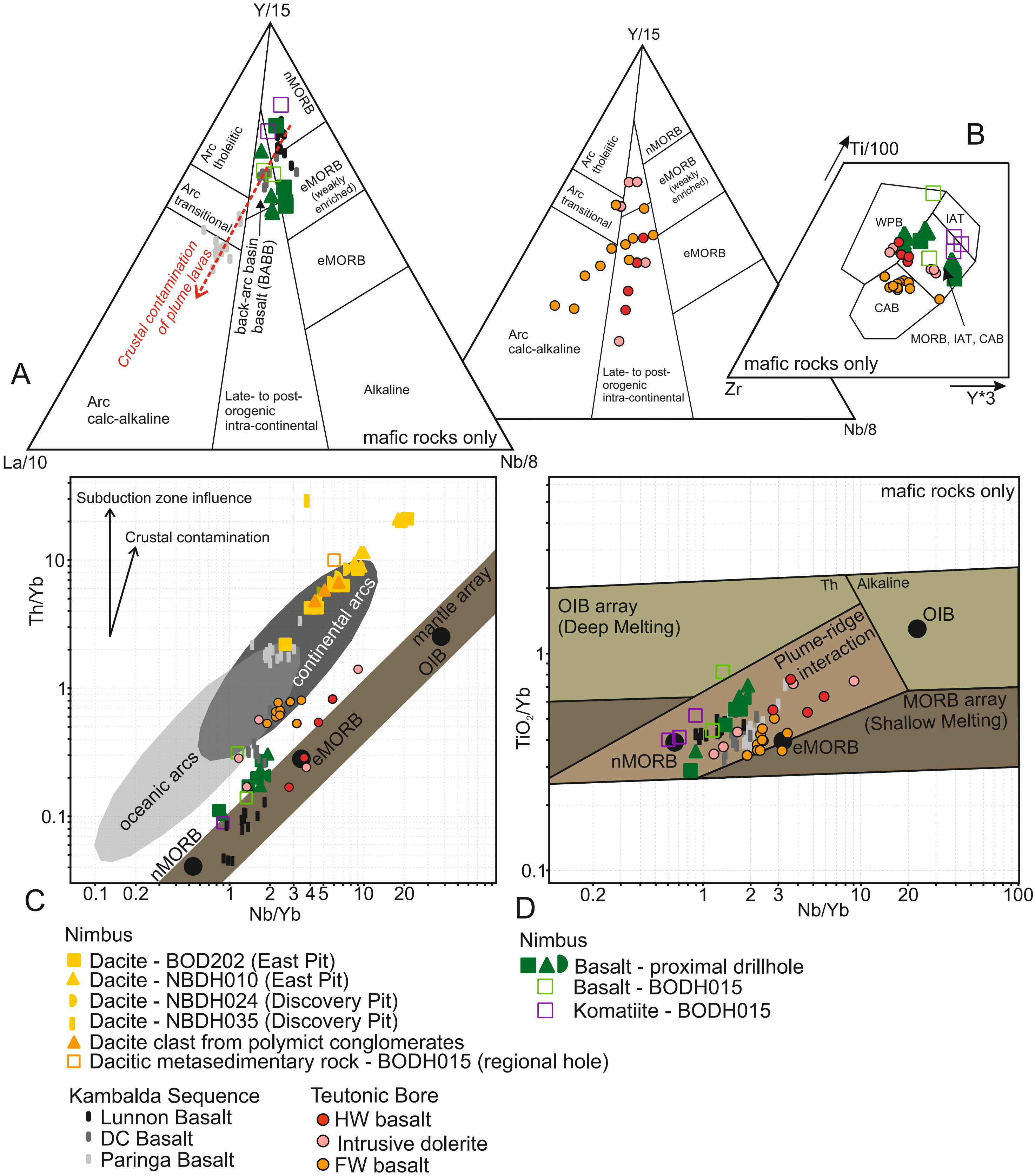

A
Y/15
La/10
Nb/8
Arc tholeiitic
Arc transitional
nMORB
eMORB (weakly enriched)
eMORB
back-arc basin basalt (BABB)
Crustal contamination of plume lavas
Arc calc-alkaline
Late- to post-orogenic intra-continental
Alkaline
mafic rocks only
Y/15
Nb/8
Arc tholeiitic
Arc transitional
nMORB
eMORB (weakly enriched)
eMORB
Arc calc-alkaline
Late- to post-orogenic intra-continental
B
Ti/100
Zr
Y*3
WPB
IAT
CAB
MORB, IAT, CAB
mafic rocks only
C
Th/Yb
Nb/Yb
Subduction zone influence
Crustal contamination
oceanic arcs
continental arcs
mantle array
OIB
eMORB
nMORB
D
TiO2/Yb
Nb/Yb
mafic rocks only
OIB array (Deep Melting)
Th
Alkaline
OIB
Plume-ridge interaction
MORB array (Shallow Melting)
nMORB
eMORB
Nimbus
Dacite - BOD202 (East Pit)
Dacite - NBDH010 (East Pit)
Dacite - NBDH024 (Discovery Pit)
Dacite - NBDH035 (Discovery Pit)
Dacite clast from polymict conglomerates
Dacitic metasedimentary rock - BODH015 (regional hole)
Kambalda Sequence
Lunnon Basalt
DC Basalt
Paringa Basalt
Teutonic Bore
HW basalt
Intrusive dolerite
FW basalt
Nimbus
Basalt - proximal drillhole
Basalt - BODH015
Komatiite - BODH015

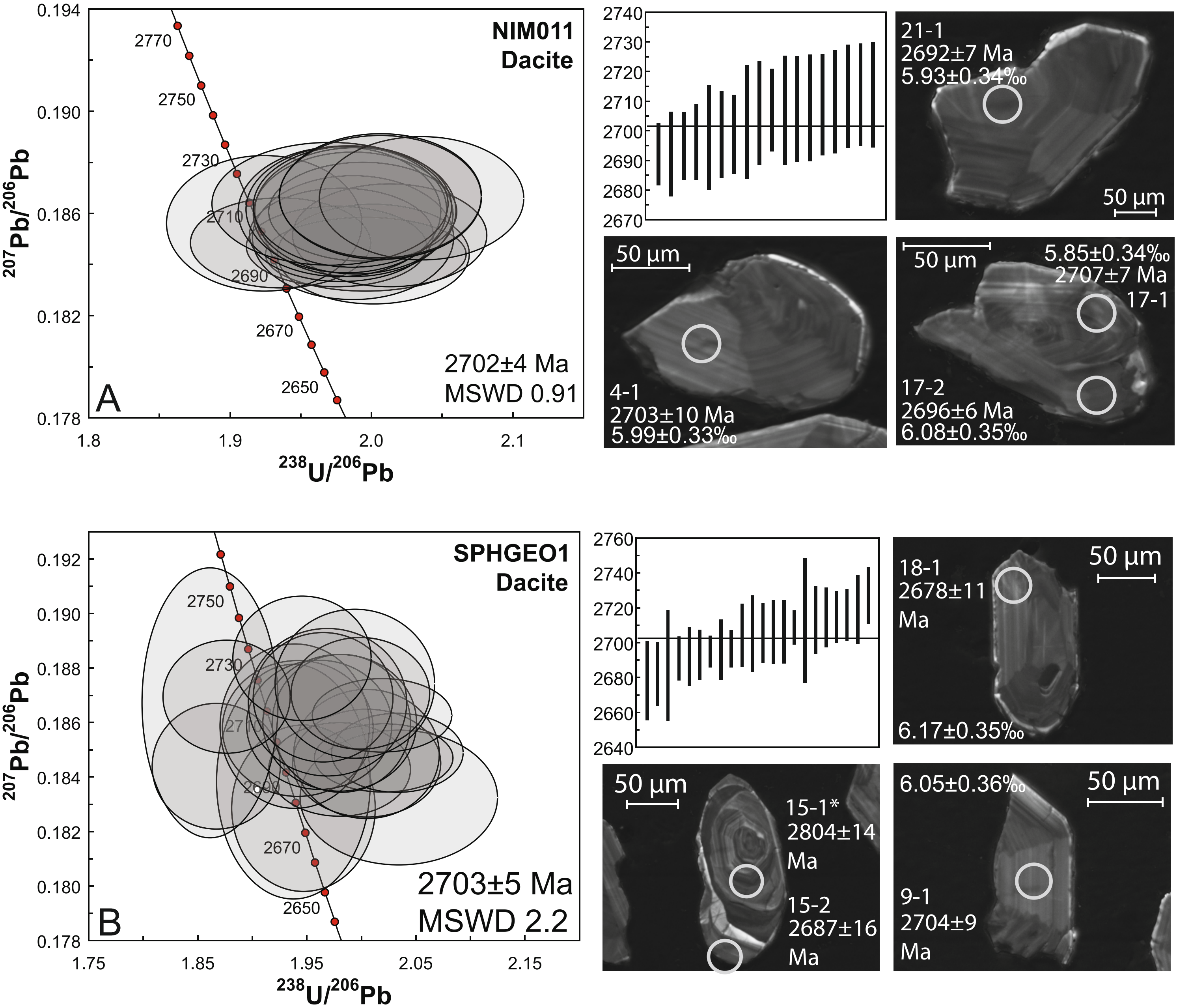

NIM011
Dacite
2702±4 Ma
MSWD 0.91
A
$^{207}Pb/^{206}Pb$
$^{238}U/^{206}Pb$
2770
2750
2730
2710
2690
2670
2650
21-1
2692±7 Ma
5.93±0.34‰
50 µm
4-1
2703±10 Ma
5.99±0.33‰
5.85±0.34‰
2707±7 Ma
17-1
17-2
2696±6 Ma
6.08±0.35‰
SPHGEO1
Dacite
2703±5 Ma
MSWD 2.2
B
18-1
2678±11
Ma
6.17±0.35‰
15-1*
2804±14
Ma
15-2
2687±16
Ma
6.05±0.36‰
9-1
2704±9
Ma

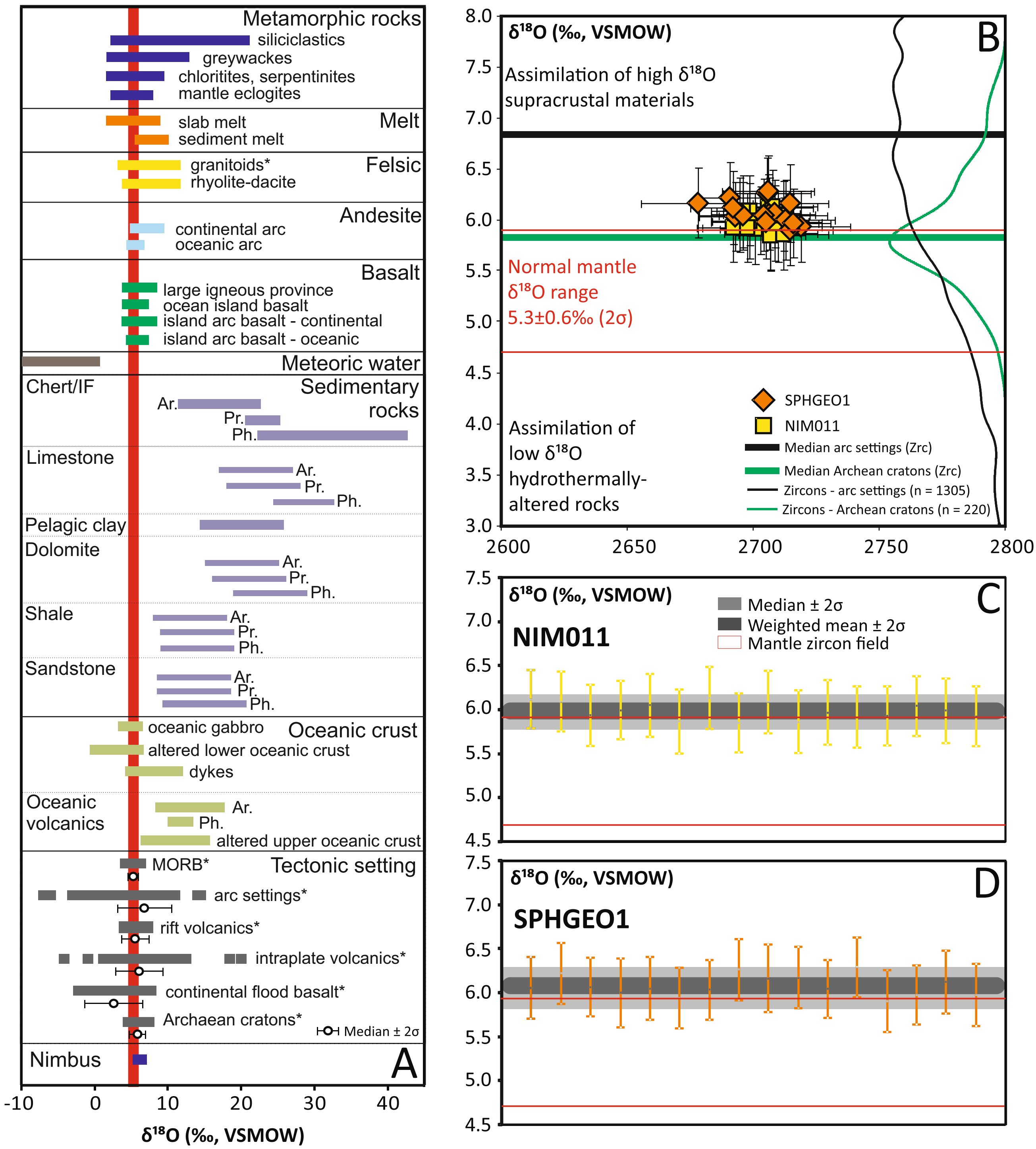

Metamorphic rocks
siliciclastics
greywackes
chloritites, serpentinites
mantle eclogites
Melt
slab melt
sediment melt
Felsic
granitoids*
rhyolite-dacite
Andesite
continental arc
oceanic arc
Basalt
large igneous province
ocean island basalt
island arc basalt - continental
island arc basalt - oceanic
Meteoric water
Chert/IF
Sedimentary rocks
Ar.
Pr.
Ph.
Limestone
Pelagic clay
Dolomite
Shale
Sandstone
oceanic gabbro
Oceanic crust
altered lower oceanic crust
dykes
Oceanic volcanics
altered upper oceanic crust
MORB*
Tectonic setting
arc settings*
rift volcanics*
intraplate volcanics*
continental flood basalt*
Archaean cratons*
Median ± 2σ
Nimbus
A
-10 0 10 20 30 40
δ18O (‰, VSMOW)
δ18O (‰, VSMOW)
B
Assimilation of high δ18O supracrustal materials
Normal mantle δ18O range 5.3±0.6‰ (2σ)
Assimilation of low δ18O hydrothermally-altered rocks
SPHGEO1
NIM011
Median arc settings (Zrc)
Median Archean cratons (Zrc)
Zircons - arc settings (n = 1305)
Zircons - Archean cratons (n = 220)
2600 2650 2700 2750 2800
δ18O (‰, VSMOW)
C
NIM011
Median ± 2σ
Weighted mean ± 2σ
Mantle zircon field
δ18O (‰, VSMOW)
D
SPHGEO1

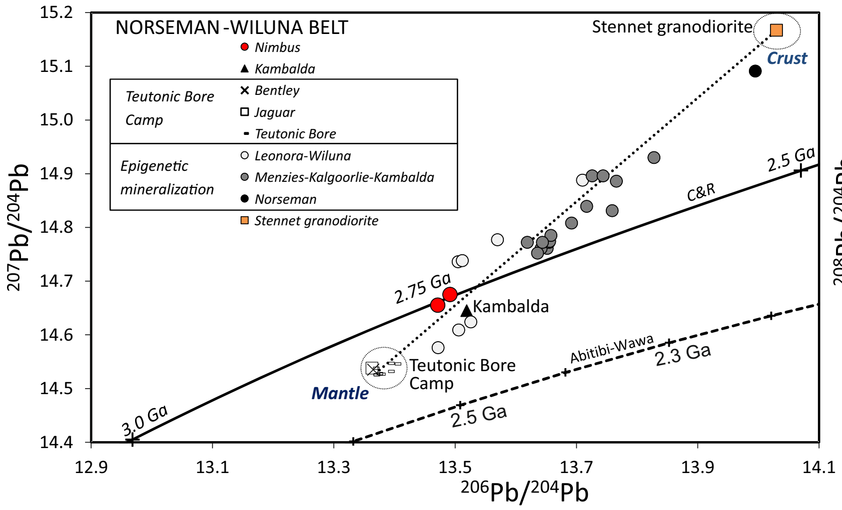
NORSEMAN -WILUNA BELT
Nimbus
Kambalda
Teutonic Bore Camp
Bentley
Jaguar
Teutonic Bore
Epigenetic mineralization
Leonora-Wiluna
Menzies-Kalgoorlie-Kambalda
Norseman
Stennet granodiorite
Stennet granodiorite
Crust
2.5 Ga
C&R
2.75 Ga
Kambalda
Teutonic Bore Camp
Mantle
Abitibi-Wawa
2.3 Ga
2.5 Ga
3.0 Ga
$^{207}Pb/^{204}Pb$
$^{206}Pb/^{204}Pb$
15.2
15.1
15.0
14.9
14.8
14.7
14.6
14.5
14.4
12.9
13.1
13.3
13.5
13.7
13.9
14.1
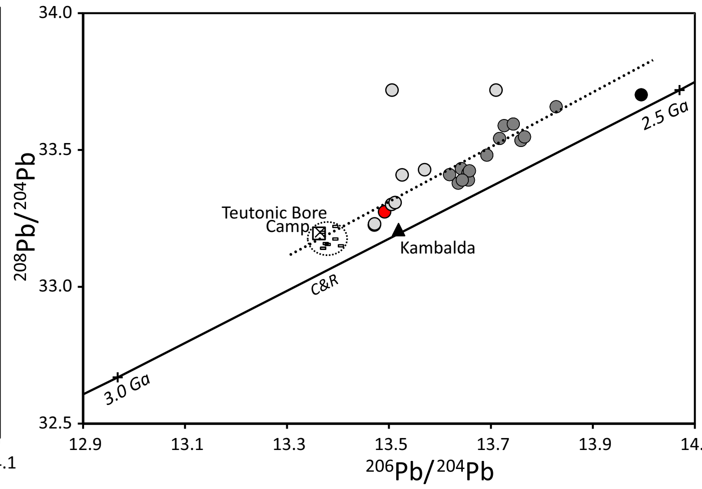
34.0
33.5
33.0
32.5
$^{208}Pb/^{204}Pb$
2.5 Ga
Teutonic Bore Camp
Kambalda
C&R
3.0 Ga
12.9
13.1
13.3
13.5
13.7
13.9
14.1
$^{206}Pb/^{204}Pb$

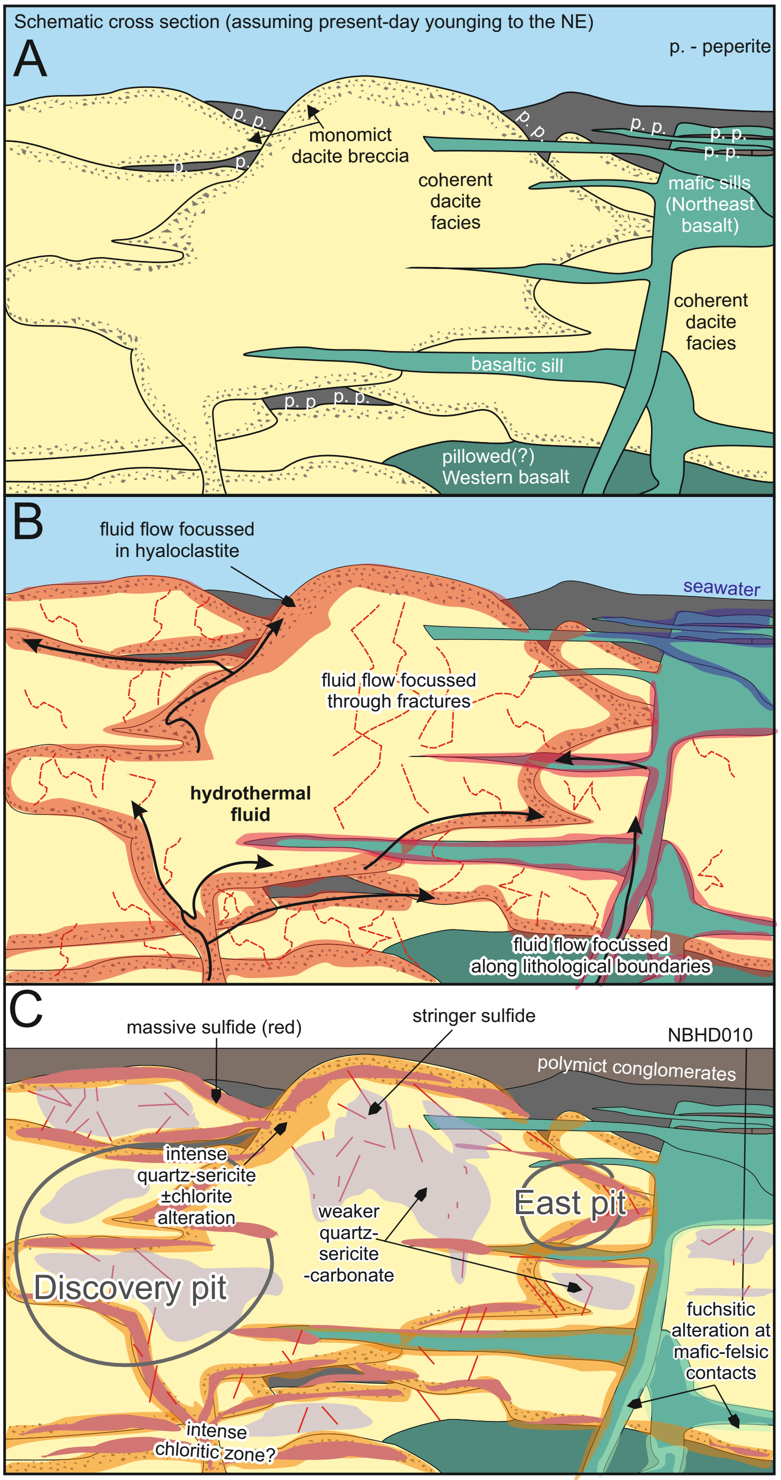

Schematic cross section (assuming present-day younging to the NE)
A
p. - peperite
p. p.
monomict dacite breccia
coherent dacite facies
mafic sills (Northeast basalt)
coherent dacite facies
basaltic sill
pillowed(?) Western basalt
B
fluid flow focussed in hyaloclastite
seawater
fluid flow focussed through fractures
hydrothermal fluid
fluid flow focussed along lithological boundaries
C
massive sulfide (red)
stringer sulfide
NBHD010
polymict conglomerates
intense quartz-sericite ±chlorite alteration
weaker quartz-sericite -carbonate
East pit
Discovery pit
fuchsitic alteration at mafic-felsic contacts
intense chloritic zone?